Contrib Mineral Petrol (2005) 149: 735–754
DOI 10.1007/s00410-005-0679-2

ORIGINAL PAPER

Dominique Lattard · Ursula Sauerzapf
Martin Käsemann

New calibration data for the Fe–Ti oxide thermo-oxybarometers from experiments in the Fe–Ti–O system at 1 bar, 1,000–1,300°C and a large range of oxygen fugacities

Received: 20 September 2004 / Accepted: 14 April 2005 / Published online: 7 June 2005

Abstract The current formulations of the Fe–Ti oxide thermobarometer (titanomagnetite–ilmenite$_{ss}$) fail to reproduce experimental results, in particular at the high temperatures that are relevant for basaltic assemblages. With the aim of improving the experimental basis of the calibration in the Fe–Ti–O system, we have synthesised assemblages of titanomagnetite–ilmenite$_{ss}$ (Tmt–Ilm$_{ss}$), ilmenite$_{ss}$–pseudobrookite$_{ss}$ (Ilm$_{ss}$–Psb$_{ss}$) and single-phase samples under a wide range of fO_2 (fixed with CO/CO_2 mixtures or by solid oxygen buffers) in sub-solidus conditions (1,000–1,300°C) at 1 bar. Runs lasted ≥24 h at 1,300°C and up to 240 h at 1,000°C and were terminated by quenching in water. All run products are polycrystalline, roughly equigranular aggregates, with grain sizes of 10–50 μm. They were examined and analysed with the SEM and EMP. Tmt compositions are broadly in accordance with the current models at moderate fO_2, but significantly richer in Ti at low fO_2 and high T, due to cationic vacancies. Ilm$_{ss}$ compositions depart from the predicted values practically at all fO_2 and T conditions, which is related to unsatisfactory thermodynamic models for the rhombohedral oxide. For Ilm$_{ss}$–Psb$_{ss}$ assemblages the best agreement between our data and current calculations is at 1,000°C and moderately high fO_2. Otherwise, experimental and calculated data strongly disagree. The experimental data set on the three Fe–Ti oxide solid solutions presented here is intended to support new versions of both the titanomagnetite–ilmenite$_{ss}$ thermo-oxybarometer and the ilmenite$_{ss}$–pseudobrookite$_{ss}$ oxybarometer.

Communicated by J. Hoefs

D. Lattard (✉) · U. Sauerzapf · M. Käsemann
Mineralogisches Institut,
Ruprecht-Karls-Universität Heidelberg,
INF 236, 69120 Heidelberg, Germany
E-mail: dlattard@min.uni-heidelberg.de
Tel.: +49-6221-544810
Fax: +49-6221-544805

Introduction

The Fe–Ti oxide thermometer and oxybarometer of Buddington and Lindsley (1964) is based on temperature and redox sensitive equilibria between titanomagnetite (Tmt; i.e. magnetite–ulvöspinel solid solution) and ilmenite–hematite solid solution (Ilm$_{ss}$). The thermo-oxybarometer enables estimates to be made of both the temperature and oxygen fugacity that prevailed during the crystallisation or re-equilibration of the Fe–Ti oxide paragenesis. The Tmt- Ilm$_{ss}$ thermo-oxybarometer was one of the first calibrated geothermometers and has been widely used to retrieve information on redox states in the Earth's mantle, processes in magma chambers, (e.g. crystallisation-differentiation, contamination or magma mixing), the crystallisation conditions of lunar or martian basalts, redox conditions during metamorphic evolution or fluid-rock interactions (e.g. Carmichael 1967; Frost 1991; Frost and Lindsley 1991; Ghiorso and Sack 1991; Haggerty 1991b; Evans and Scaillet 1997; Scaillet and Evans 1999; Herd et al. 2001, 2002; Xirouchakis et al. 2002; Devine et al. 2003).

In their pioneering work, Buddington and Lindsley (1964) presented a graphical solution of the thermo-oxybarometer that was based on the experimental results of Lindsley (1962, 1963) and applied only to parageneses within the binary Fe–Ti system. In the case of naturally occurring, multicomponent oxides a projection of their compositions into the binary system was necessary (Carmichael 1967). Subsequently, the thermo-oxybarometer has been improved in several ways: (1) supplementary calibration experiments were performed under different T–fO_2 conditions in the Fe–Ti–O system (e.g. Spencer and Lindsley 1978, 1981; Hammond et al. 1982; Simons and Woermann 1978; Andersen and Lindsley 1988) and in Mg- or Mn-bearing systems (e.g. Pinckney and Lindsley 1976); (2) projection algorithms were designed and subsequently improved (Lindsley and Spencer 1982; Stormer 1983); (3) solid solution models for titanomagnetite and ilmenite$_{ss}$ were derived on the basis

of experimental phase equilibria, magnetic and calorimetric measurements (e.g. Andersen and Lindsley 1979, 1981, 1988; Ghiorso 1990; Sack and Ghiorso 1991a) and thermodynamical formulations of the thermo-oxybarometer were developed (Powell and Powell 1977; Andersen and Lindsley 1988; Ghiorso and Sack 1991). At the same time, numerical solutions were devised to substitute for graphical interpolation and they were made available in software (Ghiorso and Carmichael 1981; Andersen and Lindsley 1988; Andersen et al. 1993; Ghiorso and Sack 1991).

At present, there are two widely used versions of the thermo-oxybarometer: (1) the one included in the QUILF package (Lindsley and Frost 1992; Frost and Lindsley 1992; Andersen et al. 1993) which utilises the solution models of Andersen and Lindsley (1988) and Andersen et al. (1991), and (2) the formulation of Ghiorso and Sack (1991) which is based on the thermodynamic analysis of the same authors and combines the solution models of Ghiorso (1990) and Sack and Ghiorso (1991a, b).

Although these two formulations are the products of sophisticated thermodynamical treatments based on sound experimental data and crystal chemical considerations, and although they have yielded a wealth of reasonable thermobarometric estimates on different volcanic suites (e.g. Ghiorso and Sack 1991; Frost and Lindsley 1992), their application does not always yield satisfactory results. Lindsley and Frost (1992) have cautioned the users of their formulation to beware of applications at oxygen fugacities higher than two log bar units above those of the fayalite–magnetite–quartz equilibrium (FMQ) (i.e. at $\Delta FMQ > 2$ or $\Delta NNO > 1.3$). Indeed, Evans and Scaillet (1997) and Scaillet and Evans (1999) showed on the basis of hydrothermal crystallisation experiments at temperatures in the range 770–870°C under controlled redox states on a dacite from Mt Pinatubo that both formulations significantly overestimate fO_2 and T (Fig. 1a, b). The temperatures calculated with the QUIlF software are typically 100°C too high and the ΔNNO values are 0.2–1 log unit above the experimental values. With the model of Ghiorso and Sack (1991), the temperature overestimates can reach 300°C (Fig. 1a, b). Discrepancies between experimental and estimated T–fO_2 conditions also occur at moderate to reduced conditions. This can be shown, for instance, from the results of crystallisation experiments at 1 bar, 1,050–1,100°C over a range of fugacities (ΔNNO −1.6 to +0.3) on a ferro-basaltic composition (Toplis and Carroll 1995). The use of the formulation of Andersen et al. (1993) leads to systematic temperature underestimates up to −180°C (Fig. 1c). The calculated ΔNNO values are in some cases correct, but in others too low by up to 0.8 log units (i.e. clearly outside the uncertainties given by the authors; cf. Andersen et al. 1993). When using the formulation of Ghiorso and Sack (1991) the calculated temperatures spread over a smaller range with positive and negative deviations (Fig. 1d). Because all synthetic Fe–Ti oxides in the studies of Scaillet and Evans (1999) and of Toplis and Carroll (1995) contain substantial amounts of supplementary elements, specifically Mg, Al, ± Mn, one may suspect that the solution models presently used do not properly account for the thermodynamic effects of these elements, in particular in the case of the rhombohedral oxides (Evans and Scaillet 1997).

Even in the simple Fe–Ti–O or Fe–Ti–Cr-O systems, the estimates with both current formulations also fail to reproduce the experimental conditions at 1,300°C (Senderov et al. 1993; Lattard 1995). At $\Delta NNO < -3$ the models predict oxygen fugacities that are much too low, and temperatures that vary from too low to too high (Fig. 1e, f) or do not yield any converging result (e.g. with the experimental data in the Cr-bearing system; Lattard 1995). This can only mean that the calibrations in the Fe–Ti–O system are not fully satisfactory. This is not that surprising, considering that very few experimental results were available at high temperatures (above 1,000°C), as well as under oxygen fugacities significantly higher or lower than those of the FMQ buffer (Fig. 2). Also note that the phase compositions in two-phase parageneses retrieved in the early 1960s may be inaccurate because without the electron microprobe and scanning electron microscope the authors had no possibility of recognizing slight chemical heterogeneities in their run products or to detect small amounts of other phases in alleged single-phase products.

Consequently, there is a strong need for more data on the compositions of coexisting titanomagnetite and ilmenite$_{ss}$ in the Fe–Ti–O system as a function of temperature (in the range 1,000–1,300°C) and oxygen fugacity (in the range ΔNNO −5 to +5). This is the main purpose of the present study. In addition, we also report compositional data for the ilmenite$_{ss}$–pseudobrookite$_{ss}$ assemblage in the same fO_2–T range because the latter paragenesis is another potential thermo-oxybarometer for oxidised terrestrial igneous rocks (Frost and Lindsley 1991; Haggerty 1991a), for some moderately reduced assemblages in mantle xenoliths (Haggerty 1991b) and for strongly reduced lunar assemblages (e.g. El Goresy et al. 1974a, b; El Goresy and Woermann 1977). Although a preliminary calibration of the Ilm$_{ss}$–Psb$_{ss}$ thermo-oxybarometer has been proposed by Anovitz et al. (1985) on the basis of thermodynamic data, the experimental data needed to refine the model are still missing.

Sub-solidus phase relations in the Fe–Ti–O system at 1 bar and T between 1,000°C and 1,300°C: a summary of previous studies

The general high-temperature, 1 bar, sub-solidus phase relations in the Fe–Ti–O system have been well established through several experimental studies, also complemented by some electrochemical measurements of the oxygen activities with zirconia cells and by a few calorimetric data (Webster and Bright 1961; Taylor 1964;

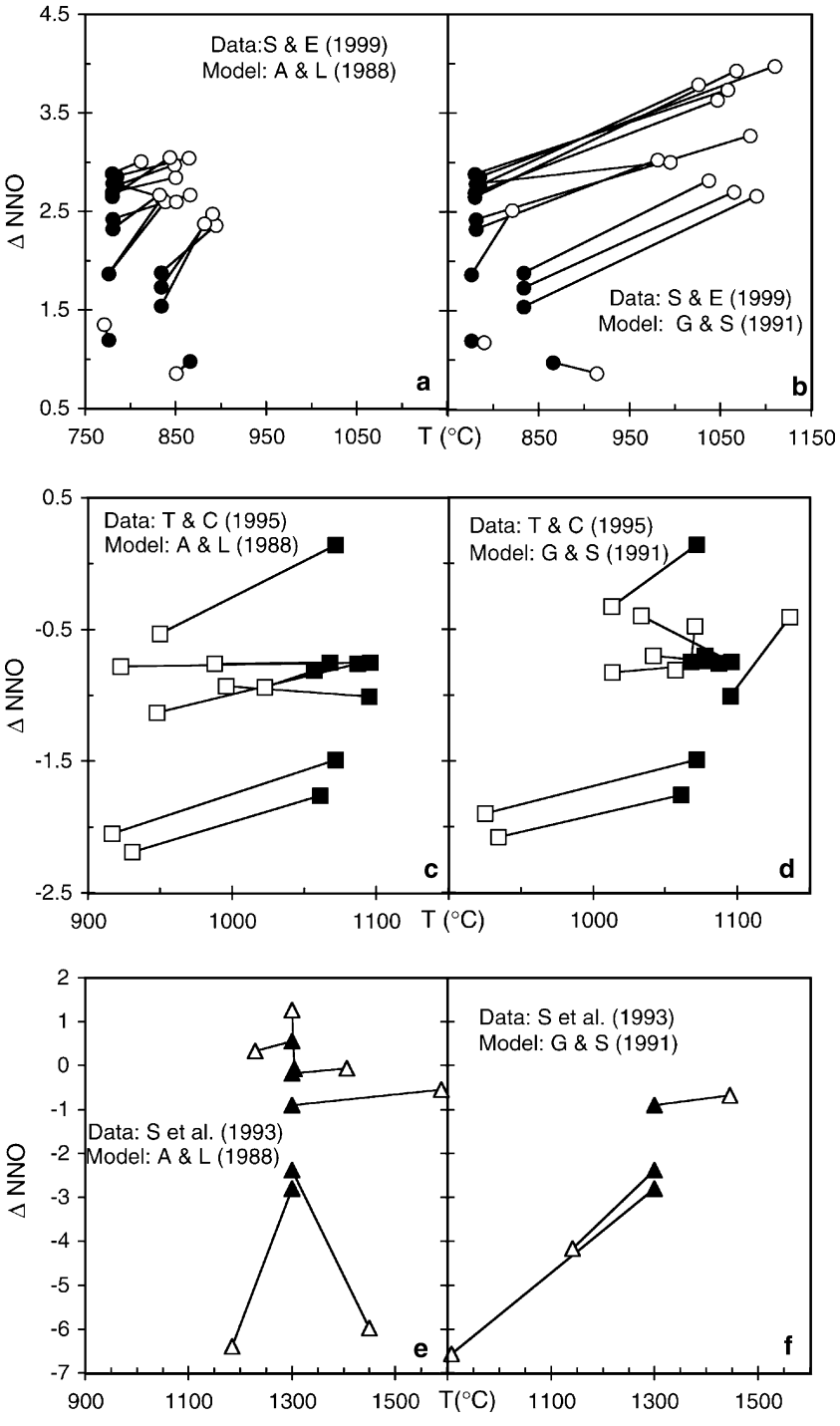

Fig. 1 Comparison of experimental (*filled symbols*) and calculated values (*open symbols*) of temperature and oxygen fugacity (expressed as ΔNNO) for Tmt–Ilm_{ss} parageneses synthesised by Scaillet and Evans (1999) (**a**, **b**), Toplis and Carroll (1995) (**c**, **d**) and Senderov et al. (1993) (**e**, **f**). Values plotted in the diagrams on the left side were calculated from the compositions of coexisting Fe–Ti oxides with the model of Andersen and Lindsley (1988), using the QUILF software (Andersen et al. 1993). In the diagrams on the right side the calculated values were retrieved with the model of Ghiorso and Sack (1991). ΔNNO = log fO_2(sample) − log fO_2(NNO-buffer). The log fO_2 values for the NNO buffer are from O'Neill and Pownceby (1993a)

Grey et al. 1974; Merritt and Turnbull 1974; Simons and Woermann 1978; Ender et al. 1980; Grey and Merritt 1981; Borowiec and Rosenqvist 1981; Anovitz et al. 1985; O'Neill et al. 1988; Woodland and Wood 1994; cf. also review of older studies in Webster and Bright 1961 and general review in Lindsley 1991).

The phase relations are dominated by three major solid-solution series (Fig. 3), the cubic spinel (titanomagnetite) series (M_3O_4) between magnetite ($Fe^{2+}Fe^{3+}_2O_4$) and ulvöspinel ($Fe^{2+}_2Ti^{4+}O_4$), the rhombohedral "α-oxide" series (M_2O_3) between hematite ($Fe^{3+}_2O_3$) and ilmenite ($Fe^{2+}Ti^{4+}O_3$), and the orthorhombic pseudobrookite series (M_3O_5) with the end-members pseudobrookite ($Fe^{3+}_2Ti^{4+}O_5$) and $Fe^{2+}Ti^{4+}_2O_5$(formerly "ferrous pseudobrookite"). All three solid solutions are essentially governed by the "ilmenite substitution", $Fe^{2+}_1Ti^{4+}_1Fe^{3+}_{-2}$. At temperatures between 1,000°C and 1,300°C, both the cubic and rhombohedral solid solutions are continuous. In the latter, however, two different structures occur, the long-range FeTi-or-

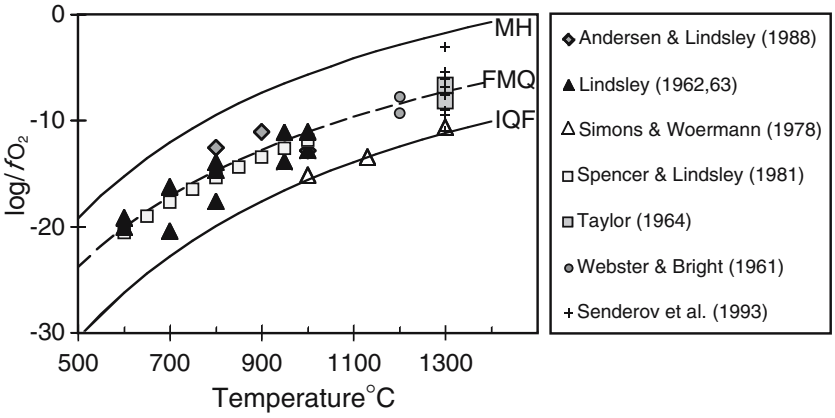

Fig. 2 log fO_2-T conditions of previous experiments on the Tmt–Ilm_{ss} thermo-oxybarometer in the Fe–Ti–O system. Pressures were between 1 bar and 2 kbar. All data, except for those of Senderov et al. (1993) (*crosses*), have been used to calibrate the models of Andersen et al. (1993) and of Ghiorso and Sack (1991). *Black curves* represent the log fO_2-T dependence of the iron–quartz–fayalite (IQF) and magnetite–hematite (MH) oxygen buffers, the *dashed curve* that of the fayalite–magnetite–quartz buffer (FMQ) (all *curves* at 1 bar; fO_2 values after O'Neill 1987 and Hemingway 1990)

dered $R\bar{3}$ structure on the side of the ilmenite end member and the long-range disordered $R\bar{3}c$ structure on the hematite side. The composition at which both structures coexist shifts from about Ilm_{70} at 1,000°C to about Ilm_{90} at 1,300°C (Harrison et al. 2000).

Only the orthorhombic series builds up a continuous solid solution towards its Ti-oxide endmember, anosovite, $Ti_2^{3+}Ti_1^{4+}O_5$, above 1,350°C (e.g. Grey and Ward 1973; Ender et al. 1980; Grey and Merritt 1981), whereby trivalent titanium is incorporated via the substitution $Fe^{2+}_{-1}Ti^{4+}_{-1}Ti^{3+}_{2}$ (e.g. Grey and Ward 1973). At $1{,}140 \pm 10$°C, $Fe^{2+}Ti_2^{4+}O_5$ decomposes to ilmenite + rutile (Haggerty and Lindsley 1969) and at temperatures between 1,140°C and 1,066°C the pseudobrookite solid solution displays two miscibility gaps (Grey and Merritt 1981). The intermediate composition, slightly richer in Ti than $Fe^{2+}Ti_2^{4+}O_5$, disappears at 1,066°C leaving one single gap between Ti_3O_5 and about $Fe^{2+}_{0.8}Fe^{3+}_{0.4}Ti^{4+}_{1.8}O_5$. The latter miscibility gap broadens towards the Fe-richer compositions with decreasing temperature and the $Fe_2^{3+}Ti^{4+}O_5$ end member breaks down to hematite + rutile at 585 ± 10°C (e.g. Haggerty and Lindsley 1969; Grey et al. 1974; Merritt and Turnbull 1974; Simons and Woermann 1978; Grey and Merritt 1981).

In contrast to the complete pseudobrookite solid solution, the rhombohedral and cubic series show only limited Ti-excess over their ferrous end members at high temperatures and low fO_2 and it is still not clear whether the excess Ti is due to Ti^{3+}. In all three series, small Ti-excess can also be related to cationic vacancies, according to a substitution of the type $Fe^{2+}_{-2}Ti^{4+}_{1}\square_1$ (Senderov et al. 1993; Lattard 1995).

Indeed, significant concentrations of cationic vacancies (i.e. up to a few per cent of the cation sum) have been detected in titanomagnetites coexisting with $ilmenite_{ss}$ in the Fe–Ti–O and in the Fe–Ti–Cr–O system (e.g. Hauptman 1974; Rahman and Parry 1978; Aragón and McCallister 1982; Dieckmann 1982; Senderov et al. 1993; Lattard 1995; Aggarwal and Dieckmann 2002). There are discrepancies between the vacancy concentrations reported by the different authors, which may partly be related to the different methods employed. In particular, the question arises whether high-temperature vacancies might be affected by the quenching procedures. Cationic vacancies might also occur at high

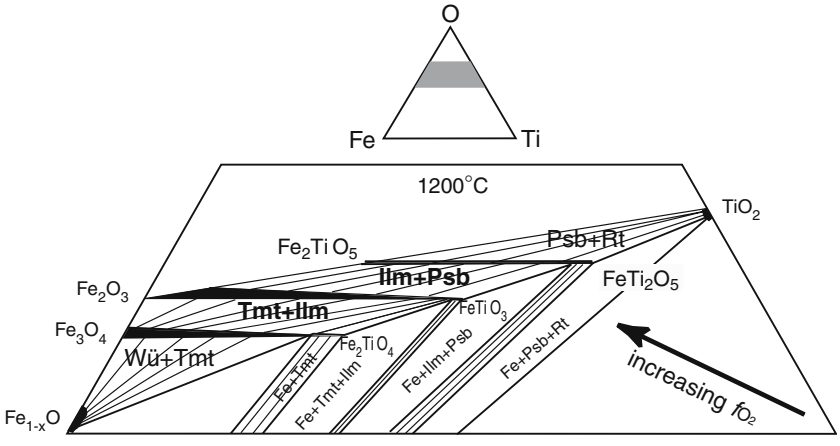

Fig. 3 Schematic phase relations in the Fe–Ti–O system at 1,200°C and 1 bar shown in part of the Fe–Ti–O triangle (modified after Grey et al. 1974; Grey and Merritt 1981). Each conode is stable only at a single fO_2 value, with fO_2 increasing from the conodes in the lower right part of the diagram (Ti-rich phase compositions) to those in the upper left part (Fe-rich phase compositions). Phase relations at very low fO_2, involving reduced rutile or other more reduced Ti oxides have been omitted (cf. Grey and Merritt 1981)

temperatures in the ilmenite and pseudobrookite solid solutions (cf. Webster and Bright 1961; Taylor 1964; Grey et al. 1974; Lattard 1995), but—to our knowledge—have not been quantified up to now.

Due to the presence of the two transition elements Fe and Ti, the phase relations among Fe–Ti oxides at 1 bar pressure are strongly dependent not only on temperature but also on oxygen fugacity. Ternary parageneses (e.g. Tmt–Ilm_{ss}–Fe°) are isobarically univariant and occur only at discrete T–fO_2 conditions. Isobarically divariant binary parageneses (e.g. Tmt–Ilm_{ss} and Ilm_{ss}–Psb_{ss}) appear over a wide range of T–fO_2 conditions (Fig. 3). At any given temperature, the compositions of Fe–Ti oxide pairs are shifted towards the Fe-rich end members with increasing oxygen fugacity, whereby titanomagnetites always have the lowest Ti/(Ti + Fe) values, ilmenites higher ones and pseudobrookites the highest (Fig. 3). With decreasing temperature the differences between the Ti/(Ti + Fe) values of the coexisting Fe–Ti oxides increase, i.e. the corresponding conodes in the Fe–Ti–O triangle become flatter. Consequently, the Tmt–Ilm_{ss} thermo-oxybarometer is based on two types of equilibria: (1) the temperature-dependent $Fe^{2+} + Ti^{4+} = 2Fe^{3+}$ exchange equilibrium which may be expressed by the reaction:

$$FeTiO_3(Ilm) + Fe_3O_4(Mag) = Fe_2O_3(Hem) + Fe_2TiO_4(Usp),$$

and (2) the oxidation of Fe^{2+} to Fe^{3+} which may be formulated by the magnetite–hematite oxygen buffer equilibrium:

$$4Fe_3O_4(Mag) + O_2 = 6Fe_2O_3(Hem).$$

Analogous equilibria hold for the Ilm_{ss}–Psb_{ss} thermo-oxybarometer.

Experimental and analytical techniques

General approach

Experiments aimed at yielding parageneses of Fe–Ti oxides with equilibrium compositions were performed at 1 bar at temperatures between 1,000°C and 1,300°C under controlled oxygen fugacities in the range ΔNNO = −5 to +5. The great majority of the experiments were sub-solidus syntheses from mixtures of Fe_2O_3 and TiO_2 in gas-mixing furnaces. In further synthesis runs at 1,000 or 1,100°C the oxygen fugacity was fixed by a solid-state oxygen buffer enclosed together with the sample in an evacuated SiO_2 glass ampoule. To check whether equilibrium was attained—or at least closely approached—in the synthesis runs, we performed parallel experiments with different bulk compositions under the same T–fO_2 and also a few re-equilibration experiments, in which the products of synthesis experiments—i.e. pairs of Fe–Ti oxides—were subsequently annealed under other T–fO_2 conditions.

The quenched run products were examined by X-ray diffraction and under a SEM to check the phase assemblages and their textures. Phase compositions were obtained from electron microprobe analyses for Ti and Fe. Oxygen was not analyzed, which means that our analytical results do not give any *direct* evidence about possible cation or oxygen vacancies.

Starting materials

For synthesis experiments, dried TiO_2 (99.9%, Aldrich Chemical Comp. Inc.), dried Fe_2O_3 (99.9%, Alpha Products), as well as dried and reduced (under H_2, 500°C) metallic iron (99 + %, Heraeus) were used for mixture preparation. Metallic iron was employed essentially in starting mixtures for experiments performed with solid oxygen buffers. In this case, the original oxygen content of the sample should be close to that of the run product because of the restricted buffer capacity.

The reagents were weighed, then ground together and mixed in an agate mortar under acetone, dried and pressed into pellets of 200–300 mg (about 5 mm diameter, 4–6 mm in length). If necessary, acetone or polyvinylalcohol was used during pressing to improve cohesion of the pellets.

For re-equilibration experiments we used fragments of pellets already crystallised to Fe–Ti oxide parageneses under other T–fO_2-conditions. These fragments were not ground prior to the re-equilibration run.

High temperature techniques

All high-temperature experiments were conducted in vertical quench furnaces, with a hot zone (±0.5°C) approximately 3 cm in length. The temperature was measured before and after the runs with a type S (Pt–$Pt_{90}Rh_{10}$) thermocouple calibrated against the melting point of silver (960.8°C) and gold (1,064.18°C). The temperature was controlled within ±0.2°C by commercial controllers. Run durations varied from 18 h at 1,300°C up to 357 h (i.e. 15 days) at 1,000°C. Experiments were terminated by quenching the run products in water.

Experiments with gas mixtures

For the gas-mixing experiments, the samples were placed on a grid of platinum wire. As sample and metal only share a very small surface and no melt ever occurs in the samples, negligible Fe-loss to the wire but maximum contact of sample with gas mixture can be achieved. Up to six pellets can be put in the furnace at once, distributed at two different levels of platinum grid with a distance of approximately 1 cm from one grid to the other.

At the beginning of the gas mixture experiments, the samples were positioned in air in the constant temperature zone of the furnace. Then, the furnace was closed and the gas flow was turned on. High-purity CO (CO > 99.97 vol.%) and CO_2 (CO_2 > 99.995 vol.%) gases were mixed with electronic valves (Millipore) and allowed to flow from the bottom to the top of the furnace tube (inner diameter 4 cm) at a rate of 200 cm^3/min. In the case of CO-rich gas mixtures, small explosions were avoided by first flushing out the air of the furnace tube with CO_2.

The oxygen fugacity was measured after the experiments with an yttria-stabilised zirconia sensor (SIRO2) with air as the reference. The sensor was tested at 1,300°C against the Ni–NiO and wüstite-magnetite equilibria. Whereas the fO_2 value bracketed for the first equilibrium matches well that of O'Neill and Pownceby (1993), the experimental results for the WM equilibrium point to a value 0.20–0.25 higher than that of O'Neill (1988), but match better the values retrieved from the equation of Darken and Gurry (1945) (reported by Huebner 1971). In fact, the WM buffer measurements of O'Neill (1988) were performed only at temperatures between 600°C and 1,000°C and—given the large non-stoichiometry of wüstite in equilibrium with magnetite, especially at high temperatures—it is doubtful whether the equation provided by this author can be adequately extrapolated to 1,300°C.

In gas mixtures with CO > 1 vol.%, the fO_2 values retrieved from the emf measurements are in general slightly higher (less than 0.2 log unit difference) than those listed in the tables of Deines et al. (1974). But, with decreasing CO content and temperature, the discrepancy between the two sets of values dramatically increases. At 1,100°C for instance, the measured fO_2 value for pure CO_2 is 1.2 log unit higher than the value calculated by Deines et al. (1974), which is probably due to the presence of O_2 as impurity in the CO_2 used (N_2 and O_2 < 25 vol pm, according to the supplier). Kress and Carmichael (1988) also noted differences between observed and predicted fO_2 values that strongly increased with increasing CO_2 proportion in the gas. Repeated long-time emf measurements have shown that gas mixtures with CO contents above 1 vol.% need less than 20 min to establish stable fO_2 values. At lower CO contents, however, up to 1 h is necessary to attain the desired fO_2 value and fluctuations can still happen thereafter. On the whole, we estimate the accuracy of the experimental fO_2 values at about ±0.2 log unit at moderate to low oxygen fugacities ($\Delta NNOfO_2$. All fO_2 values given in the following (Tables 1, 2, 3, 4, 5) are those measured with the zirconia sensor. Since we also list the CO contents of the gas mixtures, the readers can easily retrieve the fO_2 values from the tables of Deines et al. (1974) for comparison.

Run products were generally drop-quenched in water at the bottom of the furnace. In a few cases, however, the gas flow was first turned off and the samples were pulled out of the furnace and quenched in water. The whole procedure usually took less than 1 min. In the following (section "Textures of the run products") it is referred to as "slow quench".

Experiments with solid state oxygen buffers

For the solid-state buffer experiments, pellets of sample and buffer material were inserted in silica–glass tubes, which were evacuated with a rotary vane pump to a vacuum in the order of 10^{-2} mbar prior to sealing. A silica–glass filler rod was used to minimise the internal volume of the ampoule and to separate the sample from the buffer. To prevent a premature crystallisation of the ampoule during the experiments, it proved useful to heat the empty silica–glass tube and the silica-glass filler rod for several minutes with a welding torch, prior to evacuating and sealing. At the end of the experiments, the silica–glass ampoules were pulled out of the furnace and quenched in water, a procedure that lasted < 1 min.

Previous experimental studies using the silica–glass tubes technique have shown no discernable oxidation related to either leakage of the ampoule or insufficient vacuum within the ampoule (e.g. Lattard and Partzsch 2001).

Identification and chemical analysis of the run products

The phases present in the run products were identified by X-ray diffraction at room temperature with a Philips PW 3710-BASIS powder diffractometer, using Cu Kα radiation and a secondary monochromator. Sample textures were examined on polished sections with a LEO 440 scanning electron microscope.

The phases were analyzed for Fe and Ti with a Cameca electron microprobe (SX-51) operated at an acceleration voltage of 15 kV and a beam current of 20 nA. Counting times were 20 s on peak and 10 s on background. The standards used were synthetic hematite (Fe) and rutile (Ti). The raw data were corrected with the "PAP" software (Pouchou and Pichoir 1985). To avoid possible instrumental drift, calibration was checked at least every 2 h. If the measurements could not be reproduced within less than 1%, the calibration was repeated. Repeated analyses on unzoned grains show that the precision of the analyses is excellent, with 1σ standard deviations for the Ti/(Ti + Fe) values ≤0.5% (relative) (Tables 1, 2, 3, 4). Duplicate or triplicate series of analyses on about 15 samples yielded comparable Ti/(Ti + Fe) per cent values within ±0.2 at.%. Repeated analyses on a single-phase, very homogeneous ilmenite sample yielded Ti/(Ti + Fe) per cent values that differed by < 0.35 at.% from the bulk composition. Analyses performed by D.H. Lindsley at Stony Brook (using a natural ilmenite standard) on two of our Ti-rich Tmt–Ilm_{ss} run products produced only slightly higher Ti/(Ti + Fe) per cent values (difference ≤ 0.5 at.%). Therefore we think it is safe to estimate the accuracy for all

Table 1 Experiments performed at 1,300°C. Run conditions and chemical compositions of the product phases

Run no.	Bulk Ti/(Ti + Fe) at.%	T [°C]	t [h]	Redox conditions			Titanomagnetite				Rhombohedral oxide				Orthorhombic oxide			
				CO%[a]	log fO_2[b]	ΔNNO[c]	Ti/(Ti + Fe) at.%			X(Usp)[e]	Ti/(Ti + Fe) at.%			X(Ilm)[f]	Ti/(Ti + Fe) at.%			X(Fpb)[g]
							n[d]	X[d]	1σ		n	X	1σ		n	X	1σ	
6F97x0.15	3.0	1 303	24	0.2	−3.9	2.8	10	2.91	05	0.09								
6F97x1.6	3.0	1 303	23	1.6	−6.0	0.7	10	2.82	13	0.08								
6F92x1.6	8.0	1 303	23	1.6	−6.0	0.7	10	7.60	24	0.23								
6F87x1.6	13.3	1 303	23	1.6	−6.0	0.7	10	*12.92*	*52*	*0.39*								
F87 (f) 6	13.2	1 300	> 22	5.8	−7.1	−0.4	12	*13.33*	*73*	*0.40*								
6F83ax18	17.0	1 299	24	18.0	−8.3	−1.6	10	16.75	21	0.50								
6F80x18	20.0	1 299	24	18.0	−8.3	−1.6	10	20.04	18	0.60								
6F76x34	23.5	1 300	20	34.0	−9.1	−2.4	10	*23.70*	*71*	*0.71*								
6F92a	8.0	1 302	22	0.0	−3.3	3.4	10	2.86	06	0.09	12	15.19	12	0.30				
6F92x0.15	8.0	1 303	24	0.2	−3.9	2.8	10	5.38	05	0.16	10	20.96	08	0.42				
6F87x0.15	13.3	1 303	24	0.2	−3.9	2.8	10	5.38	09	0.16	10	20.96	24	0.42				
F76 (d) 6	23.5	1 300	42	0.3	−4.4	2.3	10	7.61	13	0.23	10	24.98	37	0.50				
6F80x0.5	20.0	1 301	25	0.5	−4.8	1.9	14	11.00	16	0.33	10	28.49	18	0.57				
6F76x0.5	23.5	1 301	42	0.5	−4.8	1.9	10	11.32	19	0.34	11	29.35	20	0.59				
6F80x0.75	20.0	1 301	40	0.7	−5.2	1.4	12	13.80	25	0.41	10	31.49	24	0.63				
6F76x0.75	23.5	1 301	40	0.7	−5.2	1.4	12	13.81	11	0.41	12	31.77	14	0.64				
6F72x1.5	28.0	1 302	24	1.5	−5.9	0.8	11	18.36	13	0.55	11	36.20	21	0.72				
6F69x1.5	31.0	1 302	24	1.5	−5.9	0.8	11	18.36	14	0.55	14	36.18	19	0.72				
6F76x1.6	23.5	1 303	23	1.6	−6.0	0.7	10	18.53	09	0.56	10	36.28	28	0.73				
6F72x1.6	28.0	1 303	23	1.6	−6.0	0.7	10	18.55	11	0.56	10	36.21	17	0.72				
6F69x1.6	31.0	1 303	23	1.6	−6.0	0.7	10	18.60	25	0.56	10	36.24	16	0.72				
6F72x2.4	28.0	1 299	25	2.4	−6.4	0.3	10	20.92	11	0.63	10	38.19	14	0.76				
6F67x2.4	33.0	1 299	25	2.4	−6.4	0.3	10	20.91	15	0.63	10	38.31	13	0.77				
6F72x3.4	28.0	1 299	47	3.4	−6.7	0.0	10	22.82	13	0.68	10	39.99	15	0.80				
6F69x3.4	31.0	1 299	47	3.4	−6.7	0.0	10	22.84	12	0.69	10	39.96	17	0.80				
6F72x4.4	28.0	1 300	20	4.4	−7.0	−0.3	10	24.42	13	0.73	10	41.21	21	0.82				
6IT60x4.4	40.0	1 300	20	4.4	−7.0	−0.3	10	24.46	14	0.73	10	41.52	14	0.83				
F72 (f) 6	27.6	1 300	> 24	5.8	−7.1	−0.4	10	25.32	18	0.76	10	42.61	16	0.85				
6F67x8	33.0	1 300	44	8.0	−7.4	−0.7	10	26.88	12	0.81	10	43.48	17	0.87				
6F63x8	37.0	1 300	44	8.0	−7.4	−0.7	10	27.01	22	0.81	10	43.75	21	0.88				
6F72x8R	28.0	1 300	26	8.0	−7.5	−0.8	10	27.34	17	0.82	10	44.19	16	0.88				
6F69x8R	31.0	1 300	26	8.0	−7.5	−0.8	10	27.36	12	0.82	10	44.11	15	0.88				
6F63x8R	37.0	1 300	26	8.0	−7.5	−0.8	10	27.57	11	0.83	10	44.26	18	0.89				
6F57x18R	43.3	1 301	24	18.0	−8.3	−1.6	10	30.41	13	0.91	10	47.58	20	0.95				
6F57x18	43.3	1 301	24	18.0	−8.3	−1.6	10	30.20	13	0.91	10	47.45	25	0.95				
6F63x34	37.0	1 300	> 28	34.0	−9.1	−2.4	10	32.09	10	0.96	10	48.77	13	0.98				
6F57x34	43.3	1 300	> 28	34.0	−9.1	−2.4	10	32.16	09	0.96	10	48.95	16	0.98				
6F63x34a	37.0	1 301	22	34.0	−9.1	−2.4	10	31.89	19	0.96	10	48.81	20	0.98				
6F57x34a	43.3	1 301	22	34.0	−9.1	−2.4	10	31.89	18	0.96	10	48.89	17	0.98				
6F63x66	37.0	1 299	18	66.0	−10.2	−3.5	11	34.31	16	1.03	8	50.17	24	1.00				
6F57x66	43.3	1 299	18	66.0	−10.2	−3.5	10	34.39	17	1.03	10	50.40	19	1.01				
6F57x66R	43.3	1 299	18	66.0	−10.2	−3.5	10	34.52	26	1.04	10	50.65	17	1.01				
6F83a	17.0	1 303	46	0.0	−3.3	3.4					52	16.59	12	0.33				
6F82a	18.0	1 300	51	0.0	−3.3	3.4					30	17.64	22	0.35				
6F72a	28.0	1 302	22	0.0	−3.3	3.4					12	20.50	15	0.41	11	41.26	26	0.24
6F63a	37.0	1 302	22	0.0	−3.3	3.4					12	20.92	14	0.42	9	41.39	15	0.24
6F72x0.15	28.0	1 303	24	0.2	−3.9	2.8					10	26.12	17	0.52	16	45.13	29	0.35
F57 (d) 6	43.3	1 300	24	0.3	−4.4	2.3					10	27.12	24	0.54	10	46.20	24	0.39
6F57x0.5	43.3	1 301	42	0.5	−4.8	1.9					12	31.40	13	0.63	13	49.59	17	0.49
6F57x0.75	43.3	1 301	40	0.7	−5.2	1.4					10	34.49	09	0.69	10	52.20	20	0.57
6F50x0.75	50.0	1 301	40	0.7	−5.2	1.4					10	34.76	12	0.70	10	52.44	20	0.57
6F50x1.5	50.0	1 302	24	1.5	−5.9	0.8					10	38.35	18	0.77	10	55.47	24	0.66
6F47x1.5	52.7	1 302	24	1.5	−5.9	0.8					10	38.54	12	0.77	10	55.70	15	0.67
6F50x2.4	50.0	1 299	25	2.4	−6.4	0.3					10	40.58	16	0.81	10	57.18	11	0.72
6F47x2.4	53.0	1 299	25	2.4	−6.4	0.3					10	40.44	18	0.81	10	57.28	13	0.72
6F50x4.4	50.0	1 300	20	4.4	−7.0	−0.3					10	43.35	28	0.87	10	59.76	15	0.79
6F42x4.4	58.0	1 300	20	4.4	−7.0	−0.3					10	43.41	21	0.87	10	59.80	14	0.79
F47 (f) 6	52.7	1 300	24	5.8	−7.1	−0.4					10	44.54	23	0.89	10	60.64	23	0.82
6F47x7	52.7	1 300	60	7.0	−7.2	−0.6					10	45.71	14	0.91	10	61.63	21	0.85
6F47x8	52.7	1 300	44	8.0	−7.4	−0.7					10	46.02	15	0.92	9	61.81	17	0.85

Table 1 (Contd.)

Run no.	Bulk Ti/(Ti + Fe) at.%	T [°C]	t [h]	Redox conditions			Titanomagnetite			Rhombohedral oxide				Orthorhombic oxide			
				CO%[a]	log fO_2[b]	ΔNNO[c]	Ti/(Ti + Fe) at.%		X(Usp)[e]	Ti/(Ti + Fe) at.%			X(Ilm)[f]	Ti/(Ti + Fe) at.%			X(Fpb)[g]
							n[d]	X[d] 1σ		n	X	1σ		n	X	1σ	
F47 (g) 6	52.7	1 300	25	10.3	−7.6	−0.9				11	47.29	17	0.95	13	62.51	18	0.88
F42 (g) 6	57.5	1 300	25	10.3	−7.6	−0.9				10	47.31	30	0.95	10	62.55	22	0.88
6F42x18	57.5	1 301	24	18.0	−8.3	−1.6				10	48.96	19	0.98	10	64.21	19	0.93
6F42x34	57.5	1 300	> 28	34.0	−9.1	−2.4				10	50.25	20	1.01	10	65.87	14	0.98
6F42x34a	57.5	1 301	22	34.0	−9.1	−2.4				10	50.14	17	1.00	10	65.64	25	0.97
6F42x66	57.5	1 299	18	66.0	−10.2	−3.5				10	51.80	29	1.04	10	68.23	13	1.05

[a]CO%: volume% of CO in the CO–CO_2 gas mixture
[b]log fO_2: derived from emf measurement with a zirconia cell (see Sect. 3.2.1)
[c]ΔNNO = log fO_2(experimental) − fO_2(NNO buffer). Values for NNO after O'Neill and Pownceby (1993a)
[d]X: mean over n analyses
[e]X(Usp) = 3 Ti/(Ti + Fe) [at. prop.]
[f]X(Ilm) = 2 Ti/(Ti + Fe) [at. prop.]
[g]X(Fpb) = (3 Ti/(Ti + Fe)) − 1 [at. prop.]
Values in italics refer to single-phase Tmt samples with compositional variations over the whole sample (cf. Sect. "Indications for the attainment of equilibrium")

compositions at ±0.005 for the Ti/(Ti + Fe) values, i.e. ±0.5% for the per cent values listed in Tables 1, 2, 3, 4.

Results

Textures of the run products

As planned, most run products consist of two coexisting Fe–Ti oxide phases, either Tmt + Ilm_{ss} (Fig. 4a) or Ilm_{ss} + Psb_{ss} (Fig. 4b). A few samples, however, contain only one of the three Fe–Ti oxide phases. All run products consist of polycrystalline, roughly equigranular aggregates, with grain sizes around 10–50 μm (Fig. 4).

In the two-phase samples obtained from runs with solid state buffers, the two Fe–Ti oxides are equally distributed within the whole sample. Most products of gas-mixing runs, however, display a thin outer rim (in most samples ≤100 μm, in a few cases up to 200 μm) which consists only of crystals of the Ti-richer phase, i.e. Ilm_{ss} in case of Tmt–Ilm_{ss} assemblages (Fig. 4a) and Psb_{ss} in case of Ilm_{ss}–Psb_{ss} assemblages. Such Ti-rich outer monomineralic rims appear only in run products synthesised from TiO_2 + Fe_2O_3 starting mixtures, i.e. devoid of metallic iron.

In products of gas mixing runs that were not drop-quenched, but instead more slowly pulled out of the furnace after the turning off of the CO gas, the outermost rim of the samples generally displays exsolution features in the form of very fine lamellae of Ilm_{ss} in Tmt host crystals, or of Psb_{ss} in Ilm_{ss} host crystals (Fig. 4c). Such features may appear in single-phase samples as well as in two-phase products. In the latter, they mainly affect the monomineralic rims described before (Fig. 4c). In any case, they are restricted to the outermost surface of the sample or to superficial cracks (Fig. 4c), i.e. to regions of the samples that were in contact with the surrounding gas during the "slow quench". No exsolution feature has ever been observed in the products of solid state buffer experiments in silica–glass ampoules. These observations strongly suggest that the exsolution features are related to local oxidation at the surface of the sample during the relatively long quenching procedure. They can be understood as "oxy-exsolution" features in the sense of Buddington and Lindsley (1964).

Because the outer monomineralic rims may be partially affected by the late oxidation during "slow quenching", the rims must develop earlier, i.e. during the high temperature treatment, probably in relation to elemental diffusion. This contradicts Senderov et al. (1993), who attributed these rims to quenching phenomena.

In order to avoid the possible influence of "oxy-exsolution" features, all phase compositions reported in the following have been measured on crystals from the central part of the samples (at least 200 μm away from their surfaces or from cracks).

Indications for the attainment of equilibrium

There are several good indications that the phase compositions reported in the following section reflect equilibrium conditions during the high temperature experiments.

1. In the overwhelming majority of the two-phase run products, both phases are homogeneous within the crystals and over the whole two-phase domain of the sample. This is reflected by the low 1σ standard deviations for the Ti/(Ti + Fe) values of the corresponding phases, which are below 0.5% in many samples (relative value for 10–12 single analyses; Tables 1, 2, 3, 4). Higher 1σ which reflect slightly varying compositions in neighbouring crystals, are registered only in very few two-phase products of runs at 1,000°C (Table 4). In contrast, single-phase products from gas mixture runs tend to display

Table 2 Experiments performed at 1,200°C. Run conditions and chemical compositions of the product phases

Run no.	Bulk Ti/(Ti + Fe) at.%	T [°C]	t [h]	Redox conditions			Titanomagnetite				Rhombohedral oxide				Orthorhombic oxide			
				CO%	log fO_2	ΔNNO	Ti/(Ti + Fe) at.%			X(Usp)	Ti/(Ti + Fe) at.%			X(Ilm)	Ti/(Ti + Fe) at.%			X(Fpb)
							n	X	1σ		n	X	1σ		N	X	1σ	
5F92x0.5	8.0	1 202	76	0.5	-6.2	1.6	42	7.84	11	0.24								
F87 (f) 5	13.3	1 194	48	5.4	-8.5	-0.7	16	*13.40*	*186*	*0.40*								
F87 (g) 5	13.3	1 194	48	12.5	-9.3	-1.4	14	*13.86*	*175*	*0.42*								
F72 (g) 5	27.6	1 194	48	12.5	-9.3	-1.4	15	27.72	39	0.83								
5F97a	3.0	1 201	99	0.0	-3.5	4.2	10	0.66	03	0.02	9	6.86	21	0.14				
5F87x0.25	13.0	1 201	99	0.3	-5.4	2.3	10	7.51	14	0.23	10	24.92	14	0.50				
5F87x0.5	13.3	1 202	76	0.5	-6.2	1.6	12	11.70	09	0.35	11	30.06	18	0.60				
5F76x0.5	23.5	1 202	76	0.5	-6.2	1.6	10	11.83	11	0.35	10	30.14	18	0.60				
5F72x0.5	28.0	1 202	76	0.5	-6.2	1.6	11	11.66	17	0.35	10	30.12	26	0.60				
5F76x0.65	23.5	1 201	93	0.7	-6.4	1.3	11	13.40	11	0.40	12	31.79	13	0.64				
5F72x0.65	28.0	1 201	93	0.7	-6.4	1.3	14	13.75	16	0.41	13	32.16	16	0.64				
5F72x1.25	28.0	1 200	68	1.2	-7.0	0.7	10	18.03	15	0.54	10	36.34	16	0.73				
5F69x1.25	31.0	1 200	68	1.2	-7.0	0.7	10	18.22	10	0.55	10	36.57	20	0.73				
5F69Qx2.8	31.0	1 200	68	2.8	-7.8	-0.1	10	22.12	13	0.66	10	40.08	12	0.80				
5F69Qx2.8a	31.0	1 200	> 24	2.8	-7.8	-0.1	10	22.10	15	0.66	10	40.03	16	0.80				
5F69x2.8a	31.0	1 200	> 24	2.8	-7.8	-0.1	10	21.66	11	0.65	11	39.42	18	0.79				
5F63x2.8	37.0	1 200	68	2.8	-7.8	-0.1	10	22.01	11	0.66	10	40.20	22	0.80				
5F63x2.8a	37.0	1 200	> 24	2.8	-7.8	-0.1	10	22.27	14	0.67	10	40.21	19	0.80				
F72 (f) 5	27.6	1 194	48	5.4	-8.5	-0.7	11	24.85	21	0.75	14	44.55	32	0.89				
F69 (g) 5	31.0	1 200	48	12.5	-9.3	-1.5	10	28.22	17	0.85	10	47.05	32	0.94				
5F63x33.5	37.0	1 201	52	33.5	-10.3	-2.6	10	31.12	12	0.93	10	49.02	26	0.98				
5F57x33.5	43.3	1 201	52	33.5	-10.3	-2.6	9	31.21	13	0.94	10	48.91	12	0.98				
5F60x61.5	40.0	1 200	48	61.5	-11.3	-3.6	10	32.64	15	0.98	10	49.55	19	0.99				
5F54.5x61.5	45.5	1 200	48	61.5	-11.3	-3.6	10	32.52	14	0.98	10	49.50	17	0.99				
5F60x83.5	40.0	1 200	27	83.5	-12.3	-4.6	10	34.15	09	1.02	10	50.40	21	1.01				
5F54.5x83.5	45.5	1 200	27	83.5	-12.3	-4.6	10	34.46	23	1.03	10	50.20	18	1.00				
5F92a	8.0	1 201	99	0.0	-3.5	4.2					64	7.85	10	0.16				
5F90a	10.0	1 201	53	0.0	-3.5	4.2					43	*8.99*	*84*	*0.18*				
F87(a)5	13.2	1 194	44	0.0	-3.5	4.3					10	*13.11*	*94*	*0.26*				
5F76a	23.5	1 201	68	0.0	-3.5	4.2					12	14.06	20	0.28	12	36.66	38	0.10
5F72a	28.0	1 201	68	0.0	-3.5	4.2					11	14.17	19	0.28	10	37.20	13	0.12
5F57x0.25	43.3	1 201	99	0.3	-5.4	2.3					10	28.39	29	0.57	10	47.33	24	0.42
5F57x0.5	43.3	1 202	76	0.5	-6.2	1.6					10	32.86	42	0.66	10	51.04	22	0.53
5F57x0.65	43.3	1 201	93	0.7	-6.4	1.3					10	34.81	24	0.70	10	52.55	21	0.58
5F50x0.65	50.0	1 201	93	0.7	-6.4	1.3					12	34.84	16	0.70	12	52.61	18	0.58
5F50x1.25	50.0	1 200	68	1.2	-7.0	0.7					10	39.10	00	0.78	10	56.42	11	0.69
5F47x2.8	52.7	1 200	68	2.8	-7.8	-0.1					10	43.49	11	0.87	10	58.96	22	0.77
5F47x2.8a	52.7	1 200	> 24	2.8	-7.8	-0.1					10	43.21	13	0.86	10	58.40	11	0.75
F47 (f) 5	52.7	1 200	48	4.5	-8.2	-0.5					10	46.82	32	0.94	10	60.92	24	0.83
F42 (g) 5	57.5	1 200	69	12.5	-9.3	-1.5					10	49.07	20	0.98	10	63.90	34	0.92
5F42x33.5	57.5	1 201	52	33.5	-10.3	-2.6					10	49.92	13	1.00	10	65.77	14	0.97
5F42x61.5	57.5	1 200	48	61.5	-11.3	-3.6					10	50.82	30	1.02	10	67.51	21	1.03
5F42x83.5	57.5	1 200	27	83.5	-12.3	-4.6					10	51.64	17	1.03	10	69.49	07	1.08

Same abbreviations as in Table 1

compositional variations, not within the crystals but over the whole sample. This is well documented in the product of a run at 1,300°C/NNO + 0.7, in which the titanomagnetite crystals display lower Ti contents than the bulk in the central part of the sample, but continuously rising values over the bulk in the outer, about 130 μm thick, rim of the sample (Fig. 5). Analogously, in the monomineralic rims of two-phase products (Fig. 4a) the Ti/(Ti + Fe) value of the single phase may be slightly higher than in the central (two-phase) part of the sample and even increase towards the outer surface of the sample. As shown in Fig. 6 and discussed in the following section, these different phase compositions can all represent single-phase equilibrium at the same T–fO_2 conditions, but they reflect locally different bulk compositions. Although the starting materials were thoroughly mixed, diffusion processes must occur during the high-temperature treatment in gas mixtures and lead to either Ti enrichment or Fe depletion at the surface of the sample.

2. At given T–fO_2 conditions, the phase compositions in two-phase run products are independent of the bulk composition of the sample within the permitted

Table 3 Experiments performed at 1,100°C. Run conditions and chemical compositions of the product phases

Run no.	Bulk Ti/(Ti + Fe) at.%	*T* [°C]	*t* [h]	Redox conditions			Titanomagnetite				Rhombohedral oxide				Orthorhombic oxide			
				CO%/Buffer	log fO_2	ΔNNO	Ti/(Ti + Fe) at.%			*X*(Usp)	Ti/(Ti + Fe) at.%			*X*(Ilm)	Ti/(Ti + Fe) at.%			*X*(Fpb)
							n	*X*	1σ		*n*	*X*	1σ		*n*	*X*	1 σ	
3F80x0.4	20.0	1 099	116	0.4	-7.5	1.5	13	10.43	21	0.31	14	29.58	31	0.59				
3F76x0.9	23.5	1 100	144	0.9	-8.2	0.7	11	15.95	25	0.48	9	34.84	40	0.70				
3F72x1.25	28.0	1 101	144	1.3	-8.4	0.5	10	18.56	15	0.56	10	38.41	16	0.77				
3F69x1.25	31.0	1 101	144	1.3	-8.4	0.5	10	18.52	10	0.56	10	38.23	25	0.76				
3F76Qe	24.0	1 098	120	NNO	-8.9	0.0	10	20.22	19	0.61	10	41.76	17	0.84				
3F72QNNORa	28.0	1 100	143	NNO	-8.9	0.0	10	20.54	19	0.62	10	42.00	20	0.84				
3F69Qe	31.0	1 098	120	NNO	-8.9	0.0	10	20.14	15	0.60	10	41.76	15	0.84				
F69 (e) 3	31.0	1 100	93	NNO	-8.9	0.0	10	19.99	21	0.60	10	41.85	40	0.84				
F63 (f) 3	37.0	1 100	93	FMQ	-9.7	-0.7	10	23.26	19	0.70	10	45.24	26	0.90				
F57 (X) 3	43.3	1 100	93	5.5	-9.8	-0.8	10	24.73	24	0.74	10	46.22	28	0.92				
F72 (X) 3	28.0	1 104	72	5.5	-9.8	-0.9	10	24.87	18	0.75	10	46.02	30	0.92				
F69 (X) 3	31.0	1 104	72	5.5	-9.8	-0.9	10	24.69	21	0.74	10	45.89	25	0.92				
F63 (g) 3	37.0	1 100	93	CCO	-10.4	-1.5	10	26.36	25	0.79	10	47.40	19	0.95				
3F69x16.5	31.0	1 100	135	16.5	-10.9	-2.0	10	28.35	15	0.85	9	48.06	19	0.96				
3F63x16.5	37.0	1 100	135	16.5	-10.9	-2.0	10	28.52	18	0.86	10	48.07	15	0.96				
3F69QWMR	31.0	1 100	217	WM	-11.0	-2.0	10	27.97	13	0.84	10	48.06	14	0.96				
3IT60WMa	40.0	1 101	138	WM	-11.0	-2.0	10	27.87	18	0.83	10	48.08	16	0.96				
3F57WMRc	43.3	1 100	143	WM	-11.0	-2.0	10	28.29	12	0.85	10	48.37	09	0.97				
3F65x30	35.0	1 100	96	30.0	-11.5	-2.6	10	30.07	18	0.90	10	48.76	29	0.98				
3F63x30	37.0	1 100	96	30.0	-11.5	-2.6	10	29.81	26	0.89	10	48.75	34	0.98				
3IT60IW	40.0	1 100	153	IW	-13.3	-4.4	10	32.46	16	0.97	10	49.78	10	1.00				
3F57IWR	43.3	1 100	217	IW	-13.3	-4.4	10	32.94	18	0.99	10	50.16	20	1.00				
3F97a	3.0	1 099	260	0.0	-3.7	5.3					13	3.02	10	0.06				
3P76x0	23.5	1 100	165	0.0	-3.3	5.7					10	12.31	08	0.25	10	35.84	39	0.08
3F72x0	28.0	1 100	165	0.0	-3.3	5.7					10	12.39	11	0.25	10	35.83	49	0.07
3F69x0	31.0	1 100	165	0.0	-3.3	5.7					10	12.59	17	0.25	10	35.93	42	0.08
3F57x0.4	43.3	1 099	116	0.4	-7.5	1.5					11	32.97	27	0.66	10	51.40	30	0.54
3F57x0.9	43.3	1 100	144	0.9	-8.2	0.7					9	38.05	28	0.76	11	55.11	18	0.65
3F50x1.25	50.0	1 101	144	1.3	-8.4	0.5					10	43.69	16	0.87	10	57.54	17	0.73
							Rutile											
F47 (X) 3	52.7	1 100	93	CCO	-9.8	-0.8	4	99.04	26		10	48.74	63	0.97	10	63.23	32	0.90
3F47x16.5	52.7	1 100	135	16.5	-10.9	-2.0	10	98.94	13		10	49.88	17	1.00				
3F47x30	52.7	1 100	96	30.0	-11.5	-2.6	10	99.44	11		10	50.41	38	1.01				
3F44x30	56.0	1 100	96	30.0	-11.5	-2.6	10	99.21	15		10	50.16	17	1.00				
F42 (g) 3	57.5	1 100	93	CCO	-10.4	-1.5	10	99.22	12		10	49.61	17	0.99				
3IP41IW	59.0	1 100	153	IW	-13.3	-4.4	10	99.45	08		10	51.10	17	1.02				

Same abbreviations as in Table 1
log fO_2 values for oxygen buffers: NNO (O'Neill and Pownceby 1993a), FMQ (O'Neill 1987), CCO = Co–CoO (O'Neill and Pownceby 1993a), WM and IW (O'Neill 1988)

Ti/(Ti + Fe) range. Run products with different bulk Ti/(Ti + Fe) values have only different modal proportions. This is clearly demonstrated by the results of numerous experiments in which several samples with different bulk compositions were simultaneously synthesised under given T–fO_2 conditions. These results were also reproduced in further experiments under the same T–fO_2 conditions. As documented in Tables 1, 2, 3, 4, the phase compositions measured in all products from runs under the same T–fO_2 are—except for very few cases—identical within the 1σ standard deviations.

3. We have also performed a few re-equilibration runs. Two-phase products of nine synthesis runs at different T–fO_2 conditions (Tmt–Ilm_{ss}, Ilm_{ss}–Psb_{ss} or Ilm_{ss}–Rt) were subsequently re-run at other fO_2 and/or temperatures (Table 5) to yield Tmt–Ilm_{ss} assemblages. During the re-equilibration runs at 1,300°C and ΔNNO = −0.8 the phase compositions of Tmt and Ilm_{ss} were approached from both directions (Ti-rich and Ti-poor side), i.e. a complete reversal was realised (Table 5). At 1,100°C and ΔNNO = −2.0 the Tmt composition was bracketed and the Tmt-Ilm_{ss} tie-line rotated (clockwise). The re-equilibration run at 1,100°C and ΔNNO = 0 leads to an anti-clockwise rotation of the Tmt–Ilm_{ss} tie-line. The compositions of the phases re-run at 1,300°C perfectly match those obtained from corrresponding synthesis runs (Table 1). In the products of the re-equilibration runs at 1,100°C, the phase compositions match those of

Table 4 Experiments performed at 1,000°C. Run conditions and chemical compositions of the product phases

Run no.	Bulk Ti/(Ti + Fe) at.%	T [°C]	t [h]	Redox conditions			Titanomagnetite				Rhombohedral oxide				Orthorhombic oxide			
				CO%/Buffer	log fO_2	ΔNNO	Ti/(Ti + Fe) at.%			X(Usp)	Ti/(Ti + Fe) at.%			X(Ilm)	Ti/(Ti + Fe) at.%			X(Fpb)
							n	X	1σ		n	X	1σ		n	X	1 σ	
1F92Qc	8.0	999	240	Man/H	-6.8	3.6	5	1.59	09	0.05	10	12.72	53	0.25				
1F87x0.25	13.0	999	264	0.25	-8.8	1.5	10	8.81	10	0.26	10	28.65	14	0.57				
1F80x0.25	20.0	999	264	0.25	-8.8	1.5	10	8.36	14	0.25	10	28.00	26	0.56				
F72(X)1	28.0	1 000	120	0.50	-9.3	1.0	10	12.36	27	0.37	8	32.43	41	0.65				
1F80x0.5	20.0	1 001	192	0.50	-9.3	1.0	10	12.22	13	0.37	10	32.38	16	0.65				
1F72x1	28.0	1 001	285	1.00	-10.0	0.3	10	16.57	18	0.50	10	40.43	26	0.81				
1F69x1	31.0	1 001	285	1.00	-10.0	0.3	10	16.49	11	0.49	10	40.22	17	0.80				
1F72Qe	28.0	999	192	NNO	-10.3	0.0	13	17.98	26	0.54	9	42.77	21	0.86				
F72(e)1	28.0	1 000	120	NNO	-10.3	0.0	10	17.89	22	0.54	10	42.57	14	0.85				
F63(g)1	37.0	1 000	120	CCO	-11.8	-1.5	10	24.66	24	0.74	11	47.20	77	0.94				
1P63WM	37.0	1 000	357	WM	-12.8	-2.5	10	28.09	10	0.84	10	48.93	12	0.98				
1IT60WM	40.0	1 000	357	WM	-12.8	-2.5	10	27.99	12	0.84	10	48.90	15	0.98				
1P63IW	37.0	1 001	331	IW	-14.9	-4.6	9	31.89	13	0.96	10	49.79	21	1.00				
1F57K67IW	43.0	1 001	331	IW	-14.9	-4.6	10	31.92	08	0.96	10	49.78	16	1.00				
1F57x0.25	43.3	999	264	0.25	-8.8	1.5					10	32.82	25	0.66	10	50.77	68	0.52
1F57x0.5	43.3	1 001	192	0.50	-9.3	1.0					10	38.62	21	0.77	10	53.37	62	0.60
1F47x1	52.7	1 001	285	1.00	-10.0	0.3					10	45.60	21	0.91	10	57.54	25	0.73
							Rutile											
1IP41WM	59.0	1 000	357	WM	-12.8	-2.5	10	99.50	10		10	50.40	23	1.01				
1F39IW	60.9	1 001	331	IW	-14.9	-4.6	10	99.48	10		10	50.99	29	1.02				

Same abbreviations as in Table 1
log fO_2 values for oxygen buffers: "Man/H" = MnO/Mn_3O_4 after O'Neill and Pownceby (1993b); others given in footnote of Table 3

corresponding synthesis runs (Table 3) within the uncertainties (see section "High temperature techniques").

All these considerations support the view that equilibrium was attained or at least closely approached in our synthesis and re-equilibration runs and that the phase compositions from two-phase assemblages in the central part of the samples reliably represent the corresponding T–fO_2 conditions.

Phase boundaries and compositions

The chemical compositions of the Fe–Ti oxide phases in our run products are listed together with the run

Table 5 Conditions and products of "two-steps" runs, consisting of a synthesis experiments followed by a re-equilibration run at different T–fO_2 conditions

Run no.	Bulk Ti/(Ti + Fe) (at.%)	Synthesis run								Re-equilibration run						
		T [°C]	t [h]	Redox conditions			[a]Run product	Ti/(Ti + Fe) at.%		T [°C]	t [h]	Redox conditions			[a]Run product	Ti/(Ti + Fe) at.%
				CO%/buffer	log fO_2	ΔNNO		Tmt	Ilm_{ss}			CO%/buffer	log fO_2	ΔNNO		Tmt	Ilm_{ss}
6F72x8R	28.0	1303	23	1.58	-6.0	0.7	Tmt + Ilm_{ss}	18.6	36.2	1300	26	8	-7.5	-0.8		27.3	44.2
6F69x8R	31.0	1303	23	1.58	-6.0	0.7	Tmt + Ilm_{ss}	18.6	36.2	1300	26	8	-7.5	-0.8		27.4	44.1
6F63x8R	37.0	1299	18	66.0	-10.2	-3.5	Tmt + Ilm_{ss}	34.3	50.2	1300	26	8	-7.5	-0.8		27.6	44.3
6F57x18R	43.3	999	264	0.25	-8.8	1.5	Ilm_{ss} + Psb_{ss}		32.8	1301	24	18	-8.3	-1.6		30.4	47.5
6F57x66R	43.3	1301	42	0.50	-4.8	1.9	Ilm_{ss} + Psb_{ss}		31.4	1299	18	66	-10.2	-3.5		34.5	50.7
3F72QNNORa	28.0	999	192	NNO	-10.3	0.0	Tmt + Ilm_{ss}	18.0	42.8	1100	143	NNO	-8.9	0.0		20.5	42.0
3F69QWMR	31.0	1200	> 24	2.80	-7.8	-0.1	Tmt + Ilm_{ss}	22.0	40.0	1100	217	WM	-11.0	-2.0		28.0	48.1
3F57WMRc	43.3	1301	24	18.0	-8.3	-1.6	Tmt + Ilm_{ss}	30.4	47.6	1100	143	WM	-11.0	-2.0		28.3	48.4
3F57IWR	43.3	1201	99	0.30	-5.4	2.3	Ilm_{ss} + Psb_{ss}		28.4	1100	217	IW	-13.3	-4.4		32.9	50.2

Same abbreviations as in Table 1
[a]Phase compositions are also given in Tables 1,2,3, 4, according to the temperature of the re-equilibration run

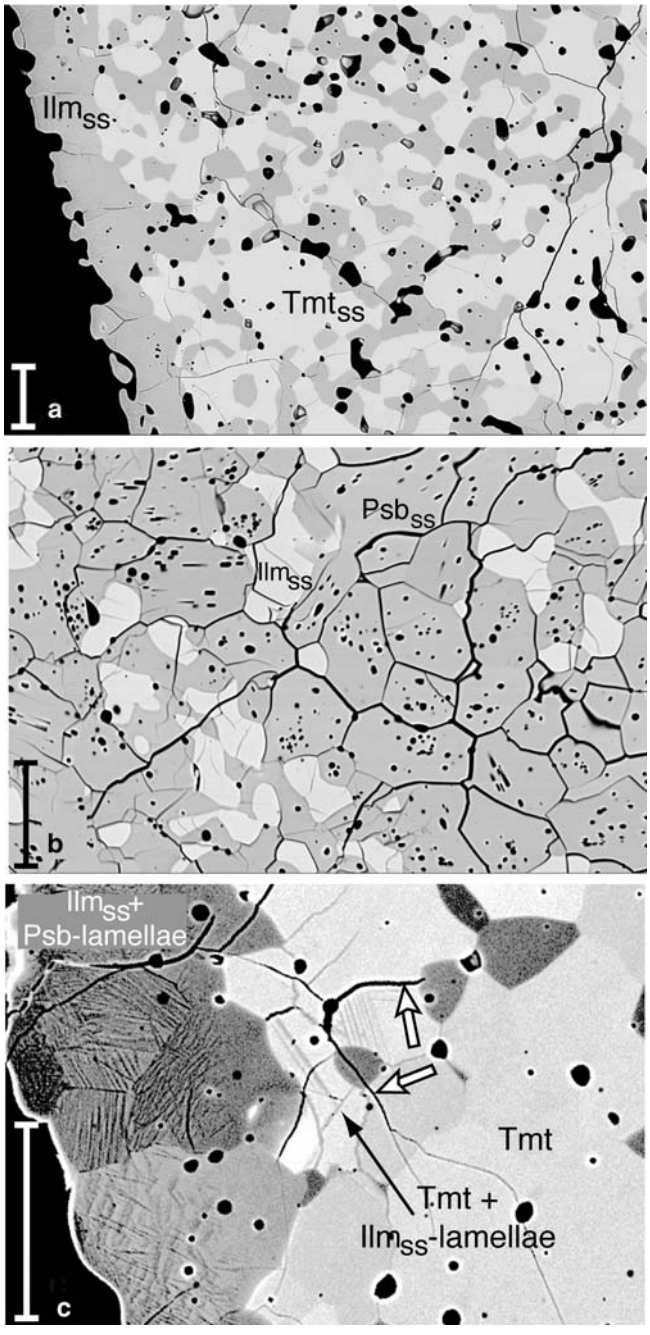

Fig. 4 Backscattered electron images of products of synthesis experiments performed in the presence of CO/CO_2 gas mixtures. All *scale bars* refer to 40 μm. **a** Two-phase sample of Tmt (X_{Usp} = 0.41; *light grey*) and Ilm_{ss} (X_{Ilm} = 0.64; *middle grey*) with a monomineralic outer rim of Ilm_{ss}. (Sample 6F76x0.75; cf. Table 1) **b** Two-phase sample of Ilm_{ss} (X_{Ilm} = 0.70; *light grey*) and Psb_{ss} (X_{Fpb} = 0.58; *middle grey*). Note the numerous negative crystal forms in the pseudobrookite$_{ss}$ grains. (Sample 5F50x0.65; cf. Table 2) **c** Two-phase sample of Tmt (X_{Usp} = 0.56; *light grey*) and Ilm_{ss} (X_{Ilm} = 0.73; *middle grey*) with a monomineralic outer rim of Ilm_{ss}. At and near the surface and along cracks developing from the surface (indicated by white arrows), Ilm_{ss} crystals have exsolved irregular Psb_{ss} lamellae (*dark grey*) and Tmt crystals have exsolved some fine rims and fine oriented lamellae of Ilm_{ss}. The contrasts have been enhanced to make the exsolution features more visible, but this results in slightly different grey tones for the single crystals of the same phase. (Sample 6F76x1.6; cf. Table 1)

conditions in Tables 1, 2, 3, 4. The Ti/(Ti + Fe) (at.%) values for all three oxides are plotted in Fig. 6 as a function of ΔNNO at the four different run temperatures, 1,000, 1,100, 1,200 and 1,300°C. These diagrams show at all temperatures the continuous shifts of the phase boundaries of the Fe–Ti oxides towards the Fe side with increasing oxygen fugacity. These shifts reflect the substitution $Fe_2^{3+}Fe_{-1}^{2+}Ti_{-1}^{4+}$.

In accordance with previous studies (e.g. Webster and Bright 1961; Taylor 1964; Senderov et al. 1993; Aggarwal and Dieckmann 2002), Tmt with very variable compositions are stable over a wide range of oxygen fugacities at all temperatures (Fig. 6). At each temperature, single-phase Tmt is stable at any given composition over 3–5 log fO_2 units. At 1300°C and fO_2 corresponding to that of the wüstite–magnetite buffer (WM) for instance, the compositional range extends from Ti/(Ti + Fe) = 0 (pure magnetite) in coexistence with wüstite up to Ti/(Ti + Fe) = 27 at.% in coexistence with $Ilm_{ss,}$ i.e. from X_{Usp} of 0 to 0.8 (Fig. 6a, Table 1). Significantly different Tmt compositions can occur in one sample under one set of T–fO_2 conditions if the

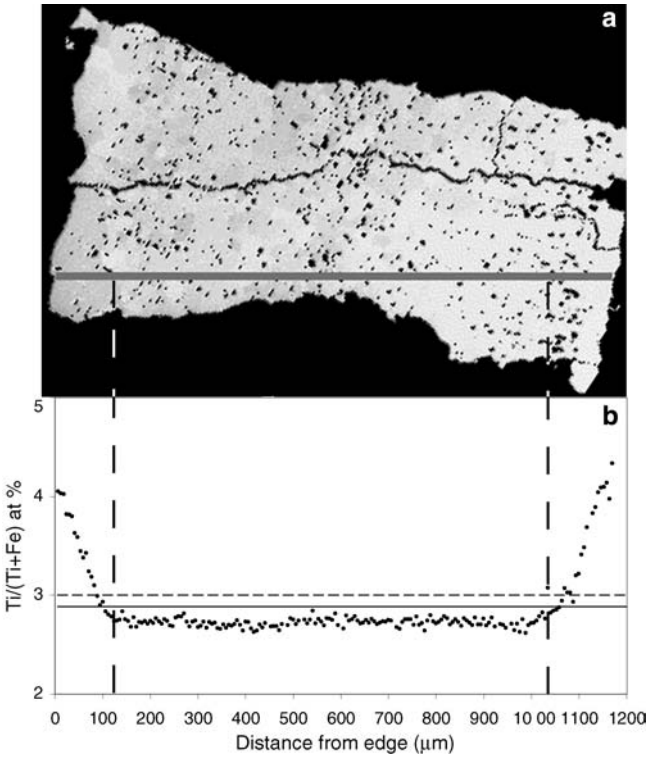

Fig. 5 Backscattered electron image (**a**) of and chemical profile (**b**) through a fragment of a single-phase, polycrystalline titanomagnetite sample, obtained from a gas mixture experiment (Sample 6F97x1.6; cf. Table 1). Note the less porous rims of about 70–100 μm thickness on the right and left side of the sample fragment. These rims represent part of the surface layer of the sample pellet, that was in contact with the gas mixture. The chemical profile reveals within these rims increasing Ti/(Ti + Fe) values towards the surface of the sample. The *horizontal solid line* represents the bulk composition of the sample, the *dashed line* the mean Ti/(Ti + Fe) of all analyses along the profile

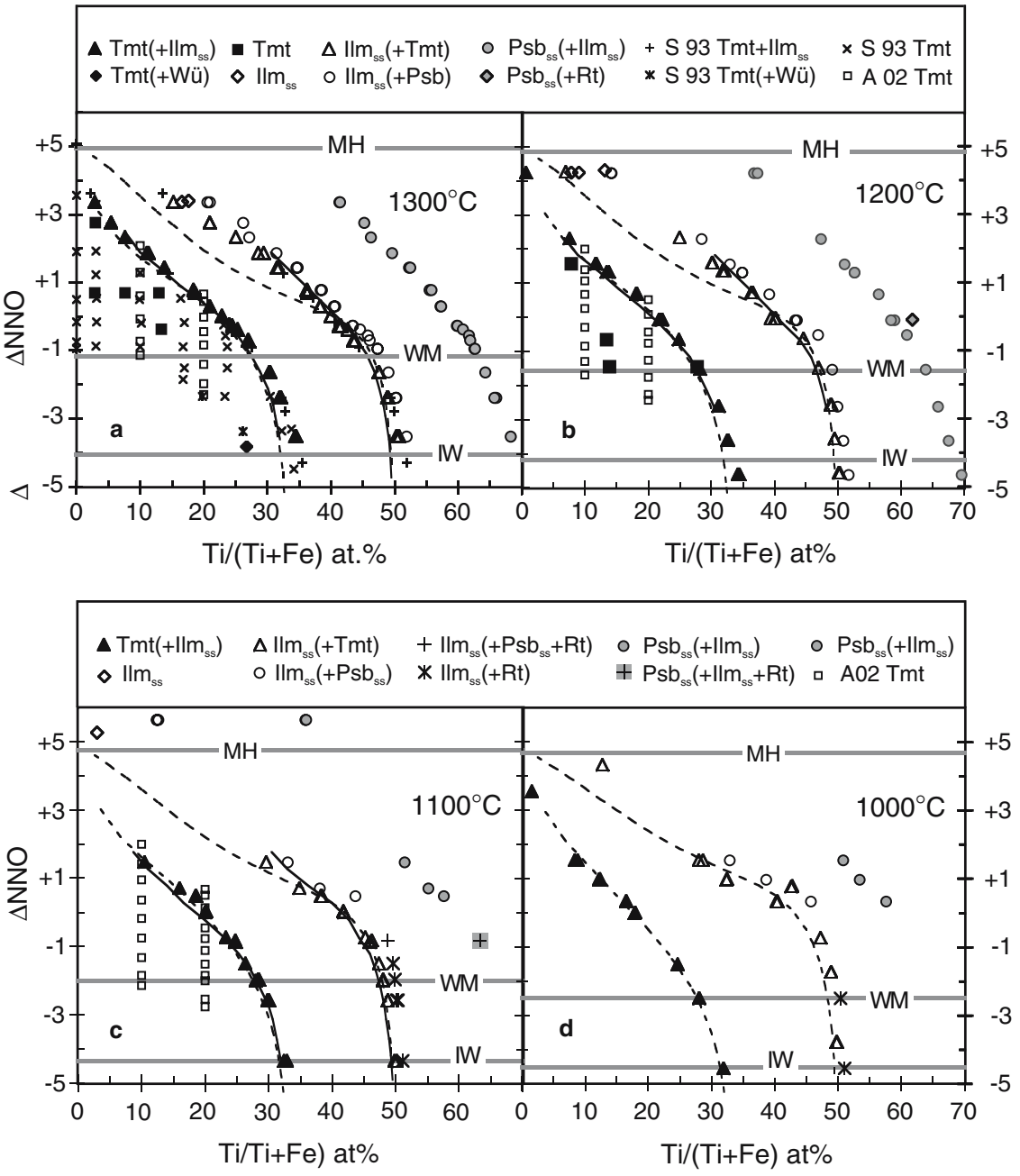

Fig. 6 Ti/(Ti + Fe) values (at.%) of titanomagnetite, ilmenite$_{ss}$ and pseudobrookite$_{ss}$ in run products as a function of temperature (**a**: 1,300°C; **b**: 1,200°C; **c**: 1,100°C; **d**: 1,000°C) and oxygen fugacity (in term of ΔNNO, as defined in the foot note of Table 1). *Triangles* represent phase compositions of coexisting Tmt (*black*) and Ilm$_{ss}$ (*open*) in two-phase run products from the present study. *Circles* are for phase compositions of coexisting Ilm$_{ss}$ (*open*) and Psb$_{ss}$ (*grey*) in two-phase run products from the present study. Most other *symbols* designate single phase products from this study or taken from Senderov et al. (1993) (S 93) or Aggarwal and Dieckmann (2002) (A 02). The *curves* represent the compositions of coexisting Tmt and Ilm$_{ss}$, as calculated from the model of Ghiorso and Sack (1991) (*solid curves*), or from the QUILF software (*dashed curves*; using the model of Andersen and Lindsley 1988)

sample displays different juxtaposed bulk compositions, as exemplified in Fig. 5.

As discussed in the literature (e.g. Hauptman 1974; Rahman and Parry 1978; Dieckmann 1982; Senderov et al. 1993; Lattard 1995; Aggarwal and Dieckmann 2002), it is clear that the large phase field of Tmt is partly related to deviations from stoichiometry. Cationic vacancies are the predominant point defects on the high fO_2 side, cation interstitials on the low fO_2 side. It must be stressed, however, that the degree of non-stoichiometry is not directly proportional to the range of oxygen fugacity under which Tmt is stable at any given

composition and temperature. In particular, this fO_2 range for a given composition changes little with temperature (Fig. 6), whereas the non-stoichiometry drastically decreases with decreasing temperature (Aggarwal and Dieckmann 2002). Research in progress already suggests that the concentration of cation vacancies is negligible at temperatures below 1100°C (Sauerzapf, pers. comm.).

In contrast to titanomagnetite, the single-phase domain of ilmenite-hematite solid solution is very restricted. At low fO_2, the Ti/(Ti + Fe) values for Ilm_{ss} in coexistence with Tmt are max. 2% lower than those of Ilm_{ss} in equilibrium with Psb_{ss} (Tables 1, 2, 3, 4; Fig. 6). The Ilm_{ss} single-phase domain broadens with increasing fO_2 and/or decreasing temperature (Fig. 6). At 1,200°C and ΔNNO = +4.2, for instance, the boundary Ti/(Ti + Fe)-values for the rhombohedral oxide are about 7% apart (Table 2, Fig. 6b).

At T≥1,200°C and ΔNNO−ss are richer in Ti than their respective Ti-bearing end members, Fe_2TiO_4 and $FeTiO_3$ (Tables 1, 2: Fig. 6a, b), in agreement with the data of Simons and Woermann (1978) and Senderov et al. (1993), but in contradiction with those of Taylor (1964). In several run products the corresponding Ti-excesses are definitely outside the estimated uncertainties of ±0.5 at.% for the Ti/(Ti + Fe) values (cf. section "Identification and chemical analysis of the run products"). Most probably, the Ti excess in both phases reflects non-stoichiometry, resulting from the $Fe^{2+}_{-2}Ti^{4+}_{1}\square_1$ substitution (Senderov et al. 1993; Lattard 1995), but it may also be related to small Ti^{3+} contents (e.g. Grey et al. 1974; Simons and Woermann 1978).

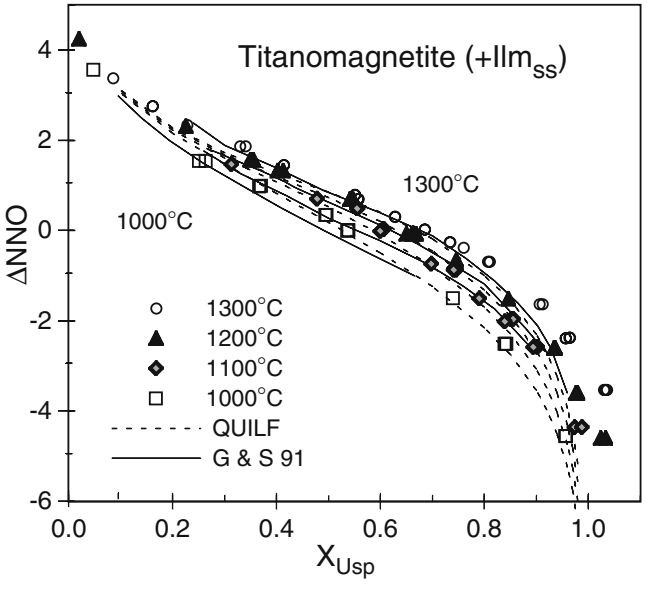

Fig. 7 Composition of titanomagnetite (X_{Usp} = mole fraction of Ulvöspinel endmember) in equilibrium with ilmenite$_{ss}$ as a function of temperature and oxygen fugacity (in term of ΔNNO). *Symbols* represent experimental data from the present study. *Solid* and *dashed curves* are isotherms calculated with the model of Ghiorso and Sack (1991) or with the QUILF software (Andersen et al. 1993; using the model of Andersen and Lindsley 1988)

A comparison of the titanomagnetite compositions (in Tmt–Ilm_{ss} assemblages) at ΔNNOFig. 7), i.e. increasing Fe^{3+} content with decreasing temperature. In case of the rhombohedral phase coexisting with titanomagnetite, the behaviour is more complex. The mineral

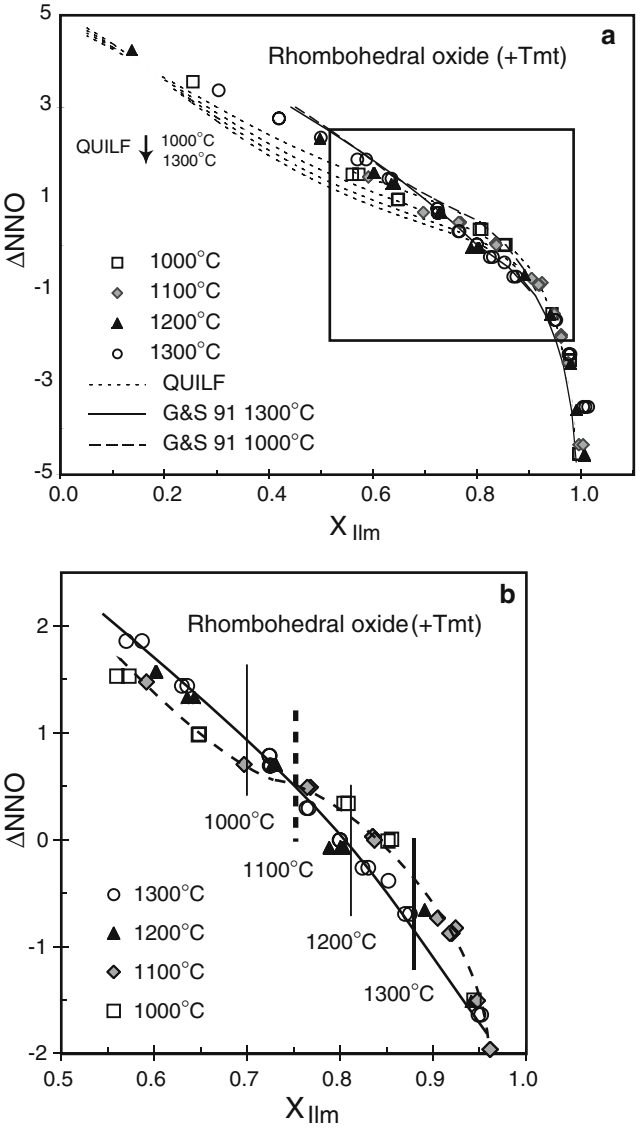

Fig. 8 **a** Composition of rhombohedral oxide (X_{Ilm} = mole fraction of Ilmenite endmember) in equilibrium with titanomagnetite as a function of temperature and oxygen fugacity (in term of ΔNNO). *Symbols* represent experimental data from the present study. *Fine dashed curves* are isotherms calculated with the QUILF software (Andersen et al. 1993; using the model of Andersen and Lindsley 1988), with the 1,300°C isotherm at the lowest ΔNNO and the 1,000°C at the highest ΔNNO values (cf. *small arrow*). *Thick solid* and *dashed curves* are the 1,300 and the 1,000°C isotherms from the model of Ghiorso and Sack (1991). **b** Close-up of the framed part of Fig. 8a. *Solid curve* is our 1,300°C isotherm, *dashed curve* our 1,100°C isotherm, both interpolated from the 1,300°C to 1,100°C experimental data of the present study (*open circles* and *grey rhombs*). The *vertical bars* point to the compositions of the rhombohedral oxide at which the transformation between the $R\bar{3}$ and the $R\bar{3}c$ structure occurs at the different temperatures (after Harrison et al. 2000)

compositions are hardly dependent on temperature, especially at low and at high fO_2 (Fig. 8a). In the middle oxygen fugacity range the isotherms present inversion points and cross over at X_{Ilm} values which correspond to the transition between the ordered $R\bar{3}$ and the disordered $R\bar{3}c$ structure (Harrison et al. 2000). This is exemplified in Fig. 8b for the 1,300 and 1,100°C isotherms.

Discussion

Comparison with previous experimental data and thermodynamic models on the titanomagnetite–ilmenite$_{ss}$ assemblage

The compositions of coexisting Tmt and Ilm$_{ss}$ retrieved from our experimental results at 1,300°C are in perfect agreement with those of Senderov et al. (1993) (Fig. 6a). The extent of the single-phase domain of Tmt is in reasonable agreement with the data of Aggarwal and Dieckmann (2002) at 1,300°C. At 1,200 and 1,100°C, however, Aggarwal and Dieckmann (2002) report for Ti/(Ti + Fe) values of 10 and 20 at.% single-phase Tmt at higher oxygen fugacities than ours (Fig. 6b, c).

Aggarwal and Dieckmann (2002) exclusively employed in-situ thermogravimetry and state that on crossing the upper fO_2 stability limit of Tmt they record a large mass change due to the oxidation of the spinel to the rhombohedral phase. Their samples were not quenched nor subsequently examined with microanalytical methods and it is not clear whether all these samples were really single-phase titanomagnetite in the reported in-situ conditions. The question especially arises for the samples equilibrated at the highest oxygen fugacities, which may have contained small amounts of the rhombohedral phase. Because the disagreement between our results and those of Aggarwal and Dieckmann (2002) strongly increases with decreasing synthesis temperature, the most probable explanation is that the samples of Aggarwal and Dieckmann (2002) did not reach equilibrium during the thermogravimetric measurements at 1,100 and 1,200°C. These authors do not report the time spans allowed for re-equilibration during their measurements.

Regarding our samples, we cannot exclude the possibility that Tmt synthesised at 1,300°C and at the upper fO_2 phase boundary might adjust to oxygen-poorer, Fe-richer Tmt with less cationic vacancies while exsolving rhombohedral oxide during quenching (cf. Figs. 6, 7). Because of the very short duration of cooling during drop-quenching, however, only extremely fine exsolution lamellae or rims of Ilm$_{ss}$ might appear within or around the titanomagnetite crystals (compare with the textures illustrated in Lattard 1995). Careful examination of all our run products with the SEM has never revealed any such feature. If these exsolution textures were so fine as to only be detectable with the TEM, they would not influence the results of our EMP analyses.

At first sight, the compositions of titanomagnetite in Tmt–Ilm$_{ss}$ assemblages are in general agreement with those retrieved from the models of Andersen and

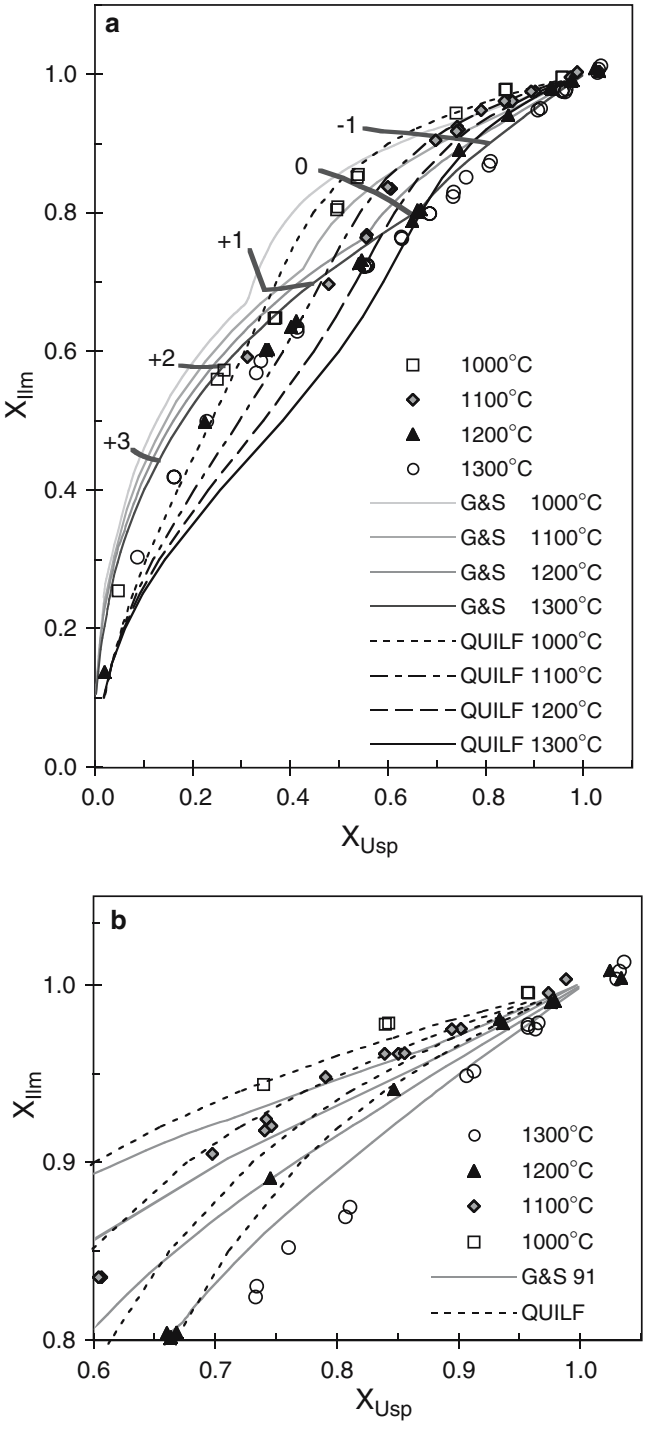

Fig. 9 **a** Roozeboom plot of coexisting rhombohedral and cubic Fe–Ti oxides from run products at different temperatures (*symbols*) compared with the isotherms calculated with the models of Ghiorso and Sack (1991) ("G&S", *grey curves*) and of Andersen & Lindsley (1988) (QUILF, *dashed curves*). Also note the iso-ΔNNO curves (*thick lines*) from Ghiorso and Sack (1991). **b** Close-up of the upper right corner of (**a**)

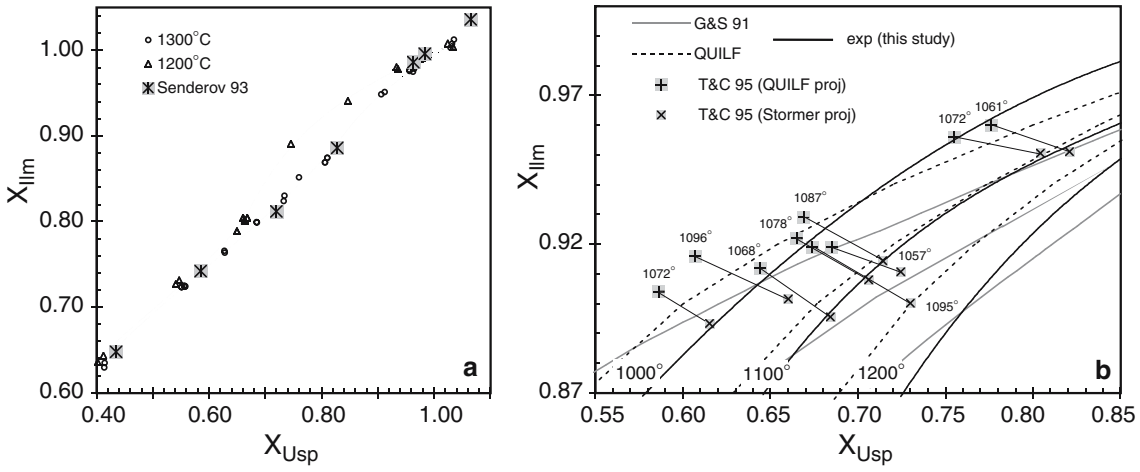

Fig. 10 **a** Roozeboom plot of coexisting rhombohedral and cubic Fe–Ti oxides from our run products at 1,300 (*circles*) and 1,200°C (*triangles*) together with data points of Senderov et al. (1993) (*crosses*). Curves represent 3rd order polynomials fits of our 1,300 and 1,200°C data points. **b** Enlarged part of the same Roozeboom diagram with the data points of Toplis and Carroll (1995) projected either according to the Andersen and Lindsley (1988) model (+ crosses, "QUILF proj", using the "NTi" and "1-Xhem" values) or with the projection scheme of Stormer (1983) (x crosses "Stormer proj"). *Thin black lines* connect the two projected points for each run product, numbers give the run temperatures. *Solid black curves* represent the 3rd order polynomial fits from our 1,200, 1,100 and 1,000°C data points. *Grey curves* are obtained from the Ghiorso and Sack (1991) model ("G&S 91"), *dashed curves* are calculated with the QUILF software (using the Andersen and Lindsley 1988 model)

Lindsley (1988) and Ghiorso and Sack (1991) (Figs. 6, 7). But a closer look at the data reveals significant discrepancies. As already discussed in the preceding section, at low oxygen fugacities and high temperatures (1,200 and 1,300°C) our synthetic titanomagnetites in equilibrium with Ilm_{ss} have especially high Ti concentrations, most probably in relation to cationic vacancies (Senderov et al. 1993; Lattard 1995). As the models do not account for vacancies, it is not surprising that they predict significantly lower Ti values. Our synthetic titanomagnetites also display higher Ti concentrations than those retrieved from the Ghiorso and Sack model at all temperatures under moderate to high oxygen fugacities ($\Delta NNO > -1$). The latter differences might reflect errors in the standard state properties used for the ulvöspinel end member.

As shown in the ΔNNO vs. Ti/(Ti + Fe) or vs. X_{Ilm} plots (Figs. 6, 8a) the variation of the Ilm_{ss} composition as a function of T and fO_2 is quite different from that calculated with the QUILF software, which is based on the model of Andersen and Lindsley (1988), especially at high oxygen fugacities and low $X_{Ilm.}$ Whereas our experimental data show practically no temperature dependence of the composition at $\Delta NNO > 1$, the isotherms of Andersen and Lindsley (1988) are shifted towards lower fugacities with increasing temperature (Fig. 8a), which means that the strongest discrepancies between experimental and calculated values are at the highest temperatures (1,300 and 1,200°C; Figs. 6a, b, 8a). On the contrary, the isotherms of Ghiorso and Sack (1991) point to higher fO_2 than our data at $\Delta NNO > 1$ (Fig. 8a). The differences in the two thermodynamic treatments of the rhombohedral oxide solid solution are even more apparent in a Roozeboom diagram of X_{Ilm} vs. X_{Usp} (Fig. 9). The smooth isotherms generated by the model of Andersen and Lindsley (1988) do not show the bend corresponding to the structural change of the rhombohedral oxide ($R\bar{3}$ to $R\bar{3}c$), which is accounted for by the isotherms of Ghiorso and Sack (1991) and which is also present in our experimental data.

In fact, it is not fair to plot values retrieved from the model of Andersen and Lindsley (1988) at $\Delta NNO > 1$ although such values can easily be obtained by using the QUILF software (Andersen et al. 1993). Andersen and Lindsley (1988) have based their solution model for the rhombohedral oxide only on compositions close to $FeTiO_3$ and did not consider the effect of the$R\bar{3}$ to $R\bar{3}c$ transition on the solution properties of the rhombohedral oxide. Consequently, they truncated their isopleth diagram at the $R\bar{3} - R\bar{3}c$ transition (cf. Figs. 2, 5 in Andersen and Lindsley 1988) and cautioned the readers that "application ... to natural samples outside the range of the experimental calibration will lead to larger uncertainties ". Lindsley and Frost (1992) did not recommend the use of the QUILF algorithms at high fO_2 conditions. Indeed, for oxidised Fe–Ti oxide parageneses that contain hematite-rich rhombohedral oxide at T > 1,000°C the mis-application of their model leads to strong underestimates of the equilibration temperatures (Fig. 9a). At somewhat lower temperatures (around 800°C), which are more relevant to relatively oxidised volcanic rocks (e.g. Pinatubo dacite, cf. Evans and Scaillet 1997; Scaillet and Evans 1999), the (mis-)use of the QUILF software yields overestimated temperatures (Fig. 1a).

The solution model for rhombohedral oxide solid solutions of Ghiorso (1990) that is incorporated in the formulation of Ghiorso and Sack (1991), does take into account the degree of long-range order and the composition-temperature dependence of the $R\bar{3}$ to $R\bar{3}c$ transition. However this model relies heavily on experi-

mental data obtained from sample compositions that could not be controlled with micro-analytical methods (e.g. Ishikawa 1958). In fact, the model does not adequately reproduce the ilmenite$_{ss}$ compositions at $\Delta NNO > 1$ (Figs. 6, 8). At any given fO_2 and T in this fugacity range, X_{Ilm} is overestimated and this is the main reason for the fO_2 overestimates for the data relevant to the Pinatubo dacite (Fig. 1b).

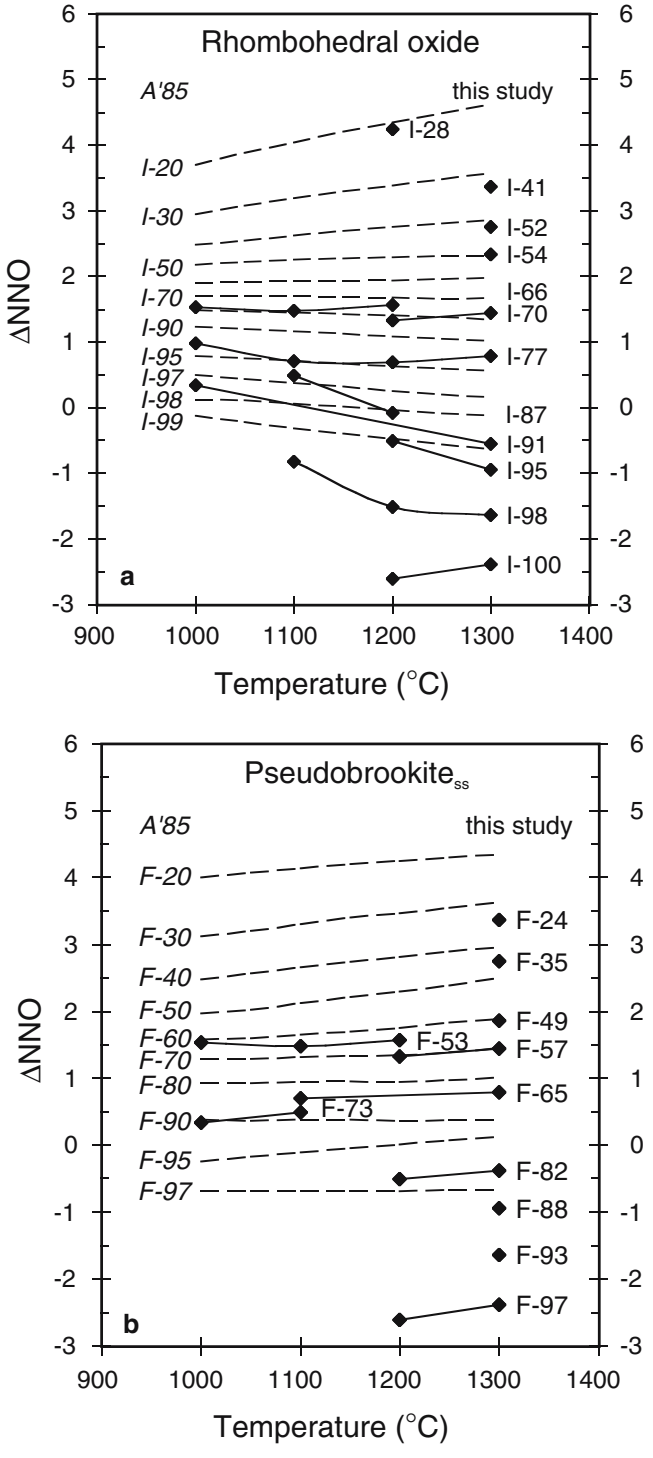

Fig. 11 Isopleths of the compositions of coexisting rhombohedral oxide (mol% $FeTiO_3$)(**a**) and pseudobrookite$_{ss}$ (mol% $FeTi_2O_5$)(**b**) as a function of temperature and oxygen fugacity (in term of ΔNNO). *Black rhombs* represent data from the present study with interpolated curves (*solid lines*). *Dashed lines* depict the data of Anovitz et al. (1985) (A′85)

In any case, it is clear that unsatisfactory thermodynamic models for the rhombohedral oxide are mainly responsible for the wrong temperature estimates for oxidised Fe–Ti oxide parageneses from the models of both Andersen and Lindsley (1988) and Ghiorso and Sack (1991). At $\Delta NNO > 1$ the modelled X_{Ilm} values are either too low (Andersen and Lindsley 1988) or too high (Ghiorso and Sack 1991), which translates into either too low or too high estimated temperatures (Figs. 8a, 9a).

In the case of moderately to highly reduced Tmt–Ilm$_{ss}$ assemblages ($\Delta NNO < 0$) the main discrepancy between experimental data and current models concern the 1,300°C results, which plot to the right, high temperature, side of the isotherms in the Roozeboom diagram (Fig. 9b). In this case, the models produce temperature overestimates. In contrast, by simply interpolating our data in the Roozeboom diagram (with 3rd order polynomials) we can well reproduce the temperatures of the experiments of Senderov et al. (1993) from the compositions of the coexisting Tmt and Ilm$_{ss}$ in their run products (Fig. 10a). The corresponding oxygen fugacities, retrieved from a polynomial interpolation of our 1,300°C data in Fig. 7, are also in excellent agreement with the experimental values of Senderov et al. (1993).

The results of our 1,100°C experiments match well with the corresponding isotherm of Andersen and Lindsley (1988) at $X_{Usp} \geq 0.65$ (Figs. 9b, 10b). Therefore, it is not clear at first sight why the experimental temperatures of Toplis and Carroll (1995) in the range 1,060–1,100°C are underestimated by the model by 100–200°C (Fig. 1c). In fact, these discrepancies are essentially caused by the algorithm used in the QUIlf software to calculate the mole fractions of the Usp and Ilm components in the Mg- and Al-bearing Tmt and Ilm$_{ss}$ (Fig. 10b). Experimental studies relevant to the petrogenesis of dacitic and andesitic magmas have shown that the projection scheme of Stormer (1983) used in conjunction with the model of Andersen and Lindsley (1988) yields more reliable temperature estimates at temperatures around 800°C and ΔNNO values around 2 (e.g. Geschwind and Rutherford 1992; Cottrell et al. 1999; Devine et al. 2003). In the T–fO_2 range of the experiments of Toplis and Carroll (1995), however, Stormer's projection leads—in conjunction both with the Andersen and Lindsley (1988) model or with our experimental isotherms—in most cases to temperature overestimates by about 20–80°C, but for the products of two runs at comparatively high fO_2 ($\Delta NNO = 0.15$ and -0.75) to underestimates in the order of 50–70°C. Apparently, neither the Andersen & Lindsley (1988) solution models nor the Stormer (1983) projection scheme are adequate for Mg- and Al-bearing Fe–Ti oxides crystallised from basaltic magmas.

Comparison with the thermodynamic model of Anovitz et al. (1985) on the Ilmenite$_{ss}$–Pseudobrookite$_{ss}$ assemblage

Some of our results on the chemical compositions of coexisting ilmenite and pseudobrookite solid solutions are plotted together with isopleths calculated by Anovitz et al. (1985) using a model based on calorimetric and phase equilibrium data. In accordance with Anovitz et al. (1985) our data show that the compositions of both phases strongly depend on the redox conditions. In contrast, the pseudobrookite compositions are practically independent of temperature and the ilmenite isopleths display a temperature dependence only at low or at very high oxygen fugacities (Fig. 11). As already noted by Anovitz et al. (1985), the Ilm$_{ss}$–Psb$_{ss}$ equilibrium is not well-suited for thermometric applications but has a good potential as an ''oxy-barometer''.

The best agreement between our data and those of Anovitz et al. (1985) is at 1,000°C and $\Delta NNO = 1.5$. At lower oxygen fugacities the model drastically overestimates fO_2 by as much as 2 log units for the most reduced conditions. At high fO_2 the model predicts too high fO_2 from the compositions of the orthorhombic oxide (Fig. 11b), but too low fO_2 from the composition of the rhombohedral oxide (Fig. 11a).

One reason for the discrepancies between our data and the model of Anovitz et al. (1985) is clearly seen in the thermodynamic treatment of the ilmenite–hematite solid solution used by the latter authors. They chose the model of Spencer and Lindsley (1981) which does not consider the effects of the $R\bar{3}$ to $R\bar{3}c$ transition, of long range order and of non-stoichiometry. On the other hand, both pseudobrookite endmembers (Fe_2TiO_5 and $FeTi_2O_5$) were treated as ordered compounds, and the solid solution was assumed to be ideal because not enough experimental data were available to sustain a more complicate model.

Perspectives for new versions of the Fe–Ti oxide thermo-oxybarometers

The experimental data set on the three Fe–Ti oxide solid solutions presented here is intended to support new versions of both the titanomagnetite–ilmenite$_{ss}$ thermo-oxybarometer and the ilmenite$_{ss}$–pseudobrookite$_{ss}$ oxybarometer.

More experimental data are currently being retrieved to quantify the concentration of cation vacancies in the Ti-rich parts of the solid solutions of both titanomagnetite and rhombohedral oxide. Supplementary results from Mg- and Al-bearing systems are also necessary to evaluate the effects of these elements on the exchange reaction. Compositional data on coexisting cubic and rhombohedral oxides in such systems are available from samples synthesised at relatively high oxygen fugacities ($3 > \Delta NNO > 0$) in the temperature and pressure range of 750–900°C and 220–390 Mpa (Scaillet and Evans 1999) and are being currently collected over a broader range of redox conditions and temperatures (Sauerzapf, pers. comm.; Evans, Scaillet and Kuehner, pers. comm.). These data will help to improve solid solution models for chemically complex titanomagnetites and rhombohedral oxides.

The present data on coexisting ilmenite$_{ss}$ and pseudobrookite$_{ss}$ in the Fe–Ti–O system yield the basis for a first experimental calibration of the corresponding oxybarometer. Fe–Mg partitioning data are known from experiments performed in the FeO–MgO–TiO_2 and Fe_2O_3–MgO–TiO_2 systems over the temperature interval 1,000–1,200°C (Pownceby and Fisher-White 1999). More partitioning data are currently being retrieved from experiments at temperatures between 1,000°C and 1,300°C under controlled oxygen fugacities in the Mg- and Al-bearing systems (Sauerzapf, pers. comm.).

Acknowledgements The Deutsche Forschungsgemeinschaft (DFG) funded this research through grant La 1164/4-1. We thank Georg Partzsch for help and advice in the high-temperature lab, Hans-Peter Meyer for maintenance of the EMP and the SEM and help during measurements at the EMP, and Michael Hanel and Ilse Glass for an initiation to and help during the use of the SEM. Technical assistance in the high-temperature and the X-ray labs was also provided by Heike Höltzen and Harry Kleinschmidt. Ilona Fin and Oliver Wienand prepared the polished sections for SEM and EMP work. Myriam Ebert, Ramona Langner, Julia Semprich and Fritz Tempelmeier assisted at different stages of this study with calculations and drafting. This work profited from frequent exchange with Ralf Engelmann (Heidelberg) and from enlightening discussions with Bernard Evans (Seattle) and Mark Ghiorso (Chicago). We thank B.R. Frost (Laramie) for a few interesting comments, M.S. Ghiorso, D.H. Lindsley (Stony Brook), H.S. O'Neill (Canberra) and especially B.W. Evans for their helpful and constructive reviews. We are particularly indebted to Don Lindsley who not only shared with us his profound knowledge on iron-titanium oxides but also took time to re-analyse some of his run products and some of ours to check for consistency. Good to know that all results are in close agreement!

References

Aggarwal S, Dieckmann R (2002) Point defects and cation tracer diffusion in $(Ti_x\ Fe_{1-x})_{3-\delta}O_4$. 1. Non-stoichiometry and point defects. Phys Chem Miner 29:695–706

Andersen DJ, Lindsley DH (1979) The olivine -ilmenite thermometer. In: Proceedings of the 10th Lun Planet Science Conference. Geochim Cosmochim Acta 11(Suppl 1):493–507

Andersen DJ, Lindsley DH (1981) A valid Margules formulation for an asymmetric ternary solution: revision of the olivine ilmenite thermometer, with applications. Geochim Cosmochim Acta 45:847–853

Andersen DJ, Lindsley DH (1988) Internally consistent solution models for Fe–Mg–Mn–Ti oxides: Fe–Ti oxides. Am Miner 73:714–726

Andersen DJ, Bishop FC, Lindsley DH (1991) Internally consistent solution models for Fe–Mg–Mn–Ti oxides: Fe–Mg–Ti oxides and olivine. Am Miner 76:427–444

Andersen DJ, Lindsley DH, Davidson PM (1993) QUILF: a Pascal program to assess equilibria among Fe–Mg–Mn–Ti oxides, pyroxenes, olivine and quartz. Comput Geosci 19:1333–1350

Anovitz LM, Treimann AH, Essene EJ, Hemingway BS (1985) The heat-capacity of ilmenite and phase equilibria in the system Fe–Ti–O. Geochim Cosmochim Acta 49:2027–2040

Aragón R, McCallister H (1982) Phase and point defect equilibria in the titanomagnetite solid solution. Phys Chem Miner 8:112–120

Borowiec K, Rosenqvist T (1981) Phase relations and oxidation studies in the system Fe–Fe_2O_3–TiO_2 at 700–1100°C. Scand J Metall 10:217–224

Buddington AF, Lindsley DH (1964) Iron-titanium oxide minerals and synthetic equivalents. J Petrol 5:310–357

Carmichael ISE (1967) The iron-titanium oxides of salic volcanic rocks and their associated ferromagnesian silicates. Contrib Mineral Petrol 14:36–64

Cottrell E, Gardner JE, Rutherford MJ (1999) Petrologic and experimental evidence for the movement and heating of the pre-eruptive Minoan rhyodacite (Santorini, Greece). Contrib Miner Petrol 135:315–331

Darken LS, Gurry RW (1945) The system iron-oxygen. I. The wüstite field and related equilibria. J Amer Chem Soc 67:1398–1412

Deines P, Nafziger RH, Ulmer GC, Woermann E (1974) Temperature-oxygen fugacity tables for selected gas mixtures in the system C–H–O at one atmosphere total pressure. Bull Earth Min Sci Exp 88:129

Devine JD, Rutherford MJ, Norton GE, Young SR (2003) Magma storage region processes inferred from geochemistry of Fe–Ti oxides in andesitic magma, Soufrière Hills Volcano, Montserrat. J Petrol 44:1375–1400

Dieckmann R (1982) Defects and cation diffusion in magnetite (IV): nonstoichiometry and point defect structure of magnetite ($Fe_{3-\delta}O_4$) 86:112–118

El Goresy A, Woermann E (1977) Opaque minerals as sensitive oxygen barometers and geothermometers in lunar basalts. In: Fraser DG (ed) Thermodynamics in geology. Reidel D, Dordrecht/Holland, pp 249–277

El Goresy A, Ramdohr P, Medenbach O, Bernhardt H-J (1974) Taurus–Littrow TiO_2-rich basalts: opaque mineralogy and geochemistry. Geochim Cosmochim Acta 1:627–652

El Goresy A, Ramdohr P, Medenbach O, Bernhardt H-J (1974) Taurus–Littrow TiO_2-rich basalts: opaque mineralogy and geochemistry. In: Proceedings of the 5th Lun Science Conference. Geochim Cosmochim Acta 5(Suppl 1):627–652

Ender A, Hofmann R, Stapper L, Dhupia G, Woermann E (1980) Die Stabilität von Pseudobrookitmischkristallen. Fortschr Miner 58(Bh1):26–28

Evans BW, Scaillet B (1997) The redox state of Pinatubo dacite and the ilmenite–hematite solvus. Am Miner 82:625–629

Frost BR (1991) Stability of oxides minerals in metamorphic rocks. In: Lindsley DH (ed) Oxide minerals: petrologic and magnetite significance, Review in Mineralogy, vol 25. Mineralogical Society of America, Washington, pp 469–483

Frost BR, Lindsley DH (1991) Occurrence of iron–titanium oxides in igneous rocks. In: Lindsley DH (ed) Oxide minerals: petrologic and magnetite significance, Review in Mineralogy, vol 25. Mineralogical Society of America, Washington, pp 433–462

Frost BR, Lindsley DH (1992) Equilibria among Fe–Ti oxides, pyroxenes, olivine, and quartz: part II. Application. Am Miner 77:1004–1020

Geschwind CH, Rutherford MJ (1992) Cummingtonite and the evolution of the Mount St. Helens (Washington) magma system: an experimental study. Geology 20:1011–1014

Ghiorso MS (1990) Thermodynamic properties of hematite–ilmenite–geikielite solid solutions. Contrib Miner Petrol 104:645–667

Ghiorso MS, Carmichel ISE (1981) A fortran IV computer program for evaluating temperatures and oxygen fugacities from the compositions of coexisting iron-titanium oxides. Comput Geosci 7:123–129

Ghiorso MS, Sack RO (1991) Fe–Ti oxide geothermometry: thermodynamic formulation and the estimation of intensive variables in silicic magmas. Contrib Miner Petrol 108:485–510

Grey IE, Merrit RR (1981) Stability relations in the pseudobrookite solid solution $Fe_yTi_{3-y}O_5$. J Solid State Chem 37:284–293

Grey IE, Ward J (1973) An X-ray and Mössbauer study of the $FeTi_2O_5$–Ti_3O_5 system. J Solid State Chem 7:300–307

Grey IE, Reid AF, Jones DG (1974) Reaction sequences in the reduction of ilmenite: 4-interpretation in terms of the Fe–Ti–O and Fe–Mn–Ti–O phase diagrams. Trans Inst Min Metall 83:105–111

Haggerty SE (1991a) Oxide textures—a mini-atlas. In: Lindsley DH (ed) Oxide minerals: petrologic and magnetite significance, Review in Mineralogy, vol 25. Mineralogical Society of America, Washington, pp 129–137

Haggerty SE (1991b) Oxide mineralogy of the upper mantle. In: Lindsley DH (ed) Oxide minerals: petrologic and magnetite significance, Review in Mineralogy, vol 25. Mineralogical Society of America, Washington, pp 355–416

Haggerty SE, Lindsley DH (1969) Stability of the Pseudobrookite (Fe_2TiO_5)–Ferropseudobrookite ($FeTi_2O_5$) Series. Carnegie Inst Washington Yearb 68:247–249

Hammond PL, Tompkins LA, Haggerty SE, Taylor SE, Spencer KJ, Lindsley DH (1982) Revised data for coexisting magnetite and ilmenite near 1000°C, NNO and FMQ buffers. GSA Meeting, Abstr Progr 14:506

Harrison RJ, Becker U, Redfern SAT (2000) Thermodynamics of the $\bar{r}^3$ to $\bar{r}^3$ phase transition in the ilmenite–hematite solid solution. Am Miner 85:1694–1705

Hauptman Z (1974) High temperature oxidation, range of non-stoichiometry and Curie point variation of cation deficient titanomagnetite. Geophys J R Astr Soc 38:29–47

Hemingway BS (1990) Thermodynamic properties for bunsenite, NiO, magnetite, Fe_3O_4, and hematite, Fe_2O_3, with comments on selected oxygen buffer reactions. Am Miner 75:781–790

Herd CDK, Papike JJ, Brearley AJ (2001) Oxygen fugacity of martian basalts from electron microprobe oxygen and TEM-EELS analyses of Fe-Ti oxides. Am Miner 86:1015–1024

Herd CDK, Borg LE, Jones JH, Papike JJ (2002) Oxygen fugacity and geochemical variations in the martian basalts: implication for martian basalt petrogenesis and the oxidation state of the upper mantle of Mars. Geochim Cosmochim Acta 66:2025–2036

Huebner JS (1971) Buffering techniques for hydrostatic systems at elevated pressures. In: Ulmer GC (ed) Research techniques for high pressure and high temperature. Springer, Berlin Heidelberg New York, pp 123–177

Ishikawa Y (1958) An order-disorder transformation phenomena in the $FeTiO_3$–Fe_2O_3 solid solution series. J Phys Soc Jpn 13:828–837

Kress VC, Carmichael ISE (1988) Stoichiometry of the iron oxidation reaction in silicate melt. Am Mineralogist 73:1267–1274

Lattard D (1995) Experimental evidence for the exsolution of ilmenite from titaniferous spinel. Am Miner 80:968–981

Lattard D, Partzsch GM (2001) Magmatic crystallization experiments at 1 bar in systems closed to oxygen: a new/old experimental approach. Eur J Miner 13:467–478

Lindsley DH (1962) Investigations in the system FeO–Fe_2O_3–TiO_2. Carnegie Inst Washington Year 61:100–106

Lindsley DH (1963) Fe–Ti oxides in rocks as thermometers and oxygen barometers. Carnegie Inst Washington Year 62:60–66

Lindsley DH (1991) Experimental studies of oxide minerals. In: Lindsley DH (ed) Oxide minerals: petrologic and magnetite significance, Review in Mineralogy, vol 25. Mineralogical Society of America, Washington, pp 69–100

Lindsley DH, Frost BR (1992) Equilibria among Fe–Ti oxides, pyroxenes, olivine, and quartz: part I. Theory. Am Miner 77:987–1003

Lindsley DH, Spencer KJ (1982) Fe–Ti oxide geothermometry: reducing analyses of coexisting Ti-magnetite (Mt) and ilmenite (Ilm). EOS 63:471

Merritt RR, Turnbull AG (1974) A solid-state cell study of oxygen activities in the Fe–Ti–O system. J Solid State Chem 10:252–259

O'Neill HSC (1987) Quartz–fayalite–iron and quartz–fayalite–magnetite equilibria and the free energy of formation of fayalite (Fe_2SiO_4) and magnetite (Fe_3O_4). Am Miner 72:67–75

O'Neill HSC (1988) Systems Fe–O and Cu–O: thermodynamic data for the equilibria Fe–''FeO'', Fe–Fe_3O_4, ''FeO''–Fe_3O_4, Fe_3O_4–Fe_2O_3, Cu–Cu_2O, and Cu_2O–CuO from emf measurements. Am Miner 73:470–486

O'Neill HSC, Pownceby MI (1993a) Thermodynamic data from redox reactions at high temperatures. I. An experimental and theoretical assessment of the electrochemical method using stabilized zirconia electrolytes, with revised values for the Fe–''FeO'', Co–CoO, Ni–NiO and Cu–Cu_2O oxygen buffers, and new data for the W–WO_2 buffer. Contrib Miner Petrol 114:296–314

O'Neill HSC, Pownceby MI (1993b) Thermodynamic data from redox reactions at high temperatures. II. The MnO–Mn_3O_4 oxygen buffer, and implications for the thermodynamic properties of MnO and Mn_3O_4. Contrib Miner Petrol 114:315–320

O'Neill HSC, Pownceby MI, Wall VJ (1988) Ilmenite–rutile–iron and ulvöspinel–ilmenite–iron equilibria and the thermochemistry of ilmenite ($FeTiO_3$) and ulvospinel (Fe_2TiO_4). Geochim Cosmochim Acta 52:2065–2072

Pinckney LR, Lindsley DH (1976) Effects of magnesium on iron-titanium oxides. GSA Meeting, Abstr Progr 8:1051

Pouchou JL, Pichoir F (1985) 'PAP' $\phi(\rho Z)$ procedure for improved quantitative microanalysis. Microbeam Anal 1985:104–106

Powell R, Powell M (1977) Geothermometry and oxygen barometry using coexisting iron-titanium oxides: a reappraisal. Miner Mag 41:257–263

Pownceby MI, Fisher-White MJ (1999) Phase equilibria in the systems Fe_2O_3–MgO–TiO_2 and FeO–MgO–TiO_2 between 1173 K and 1473 K, and Fe^{2+} –Mg mixing properties of ilmenite, ferrous-pseudobrookite and ulvöspinel solid solutions. Contrib Miner Petrol 135:198–211

Rahman AA, Parry LG (1978) Titanomagnetites prepared at different oxidation conditions: hysteresis properties. Phys Earth Planet Inter 16:232–239

Sack RO, Ghiorso MS (1991a) An internally consistent model for the thermodynamic properties of Fe–Mg–titanomagnetite–aluminate spinels. Contrib Miner Petrol 106:474–505

Sack RO, Ghiorso MS (1991b) Chromian spinels as petrogenetic indicators: thermodynamics and petrological applications. Am Miner 76:827–847

Scaillet B, Evans B (1999) The 15 June 1991 eruption of Mount Pinatubo. I. Phase equilibria and pre-eruption P–T—fO_2–fH_2O conditions of the dacite magma. J Petrol 40:381–411

Senderov E, Dogan AU, Navrotsky A (1993) Nonstoichiometry of magnetite-ulvöspinel solid solutions quenched from 1,300°C. Am Miner 78:565–573

Simons B, Woermann E (1978) Iron titanium oxides in equilibrium with metallic iron. Contrib Miner Petrol 66:81–89

Spencer KJ, Lindsley DH (1978) New experimental results on the magnetite–ulvöspinel, hematite–ilmenite solution model using the CoCoO buffer. GSA Abstr Progr 10:496

Spencer KJ, Lindsley DH (1981) A solution model for coexisting iron-titanium oxides. Am Miner 66:1189–1201

Stormer JCJ (1983) The effects of recalculation on estimates of temperature and oxygen fugacity from analyses of multicomponent iron-titanium oxides. Am Miner 68:286–594

Taylor RW (1964) Phase equilibria in the system FeO–Fe_2O_3–TiO_2 at 1300°C. Am Miner 49:1016–1030

Toplis MJ, Carroll MR (1995) An experimental study of the influence of oxygen fugacity on Fe–Ti oxide stability, phase relations, and mineral–melt equilibria in ferro–basaltic systems. J Petrol 36:1137–1170

Webster AH, Bright NFH (1961) The system Iron–Titanium–Oxygen at 1,200°C and oxygen partial pressures between 1 atm. and 2×10^{-14} atm.. J Am Ceram Soc 44:110–116

Woodland AB, Wood BJ (1994) Fe_3O_4 activities in Fe–Ti spinel solid solutions. Eur J Miner 6:23–37

Xirouchakis D, Draper DS, Schwandt CS, Lanzirotti A (2002) Crystallization conditions of Los Angeles, a basaltic Martian meteorite. Geochim Cosmochim Acta 66:1867–1880